

Langevin treatment of quantum fluctuations and optical patterns in optical parametric oscillators below threshold

A. Gatti,* H. Wiedemann,* L. A. Lugiato, and I. Marzoli

Istituto Nazionale per la Fisica della Materia, Dipartimento di Fisica, Università degli Studi di Milano, Via Celoria 16, 20133 Milano, Italy

Gian-Luca Oppo[†] and Stephen M. Barnett

Department of Physics and Applied Physics, University of Strathclyde, 107 Rottenrow, Glasgow G4 0NG, Scotland, United Kingdom

(Received 25 November 1996)

A Langevin model is introduced to study quantum fluctuations below the threshold of pattern formation for optical parametric oscillators (OPO's). In particular we compare analytical and numerical results for the OPO with one and two transverse spatial dimensions and in the presence of either plane or spherical cavity mirrors. The far-field structure and the correlation functions of the fluctuating signal field anticipate the onset of a transverse spatial pattern which arises classically even in the presence of Gaussian input beams. Correlation functions also reveal the squeezed nature of the OPO field. Numerical simulations of the Langevin model describe the result of short time measurements and show that close to threshold the near-field signal is a noisy spot pattern evolving on a time scale longer than the inverse decay rate of the resonator. This and other far-field features should be experimentally accessible. [S1050-2947(97)02907-7]

PACS number(s): 42.50.Dv, 42.65.-k

I. INTRODUCTION

Although the generation of the so-called nonclassical light [1–3] and the formation of transverse spatial patterns [4–6] are two widely analyzed phenomena in quantum and nonlinear optics, they are usually studied separately. Theoretical treatments of the quantum statistics of the output of nonlinear optical systems are usually restricted to the framework of the plane wave approximation, apart from few exceptions [7–9]. In contrast, studies of nonlinear optical patterns take into account transverse variations of the optical fields but are usually confined to the semiclassical description. Unlike other disciplines (such as hydrodynamics and chemical reactions) where a classical description of pattern formation is sufficient, optical systems may show noteworthy quantum aspects at room temperature [10]. Only recently have attempts been made to combine these two aspects of nonlinear optical systems into a general framework [11–16].

A prominent model for the generation of squeezed light as well as for the formation of spatial patterns [17] is the optical parametric oscillator (OPO) which is therefore a natural choice to study the interrelation of quantum fluctuations and optical patterns. At degeneracy, OPO's generate light of a frequency ω_s (signal) from injected light of frequency $2\omega_s$ (pump). We discuss here three different configurations of the OPO: with plane mirrors and a homogeneous input beam, with plane mirrors and an input beam of finite diameter, and with spherical mirrors and a homogeneous input beam. For all these realizations the semiclassical OPO models exhibit a second-order phase transition from zero to finite signal field

for appropriate threshold parameters, similar to what one has in lasers [18,19]. Furthermore, when diffraction is taken into account, both signal and pump exhibit a transverse spatial pattern at threshold under appropriate operating conditions [17]. In recent publications it was shown that these semiclassical patterns are anticipated in the quantum correlation functions in the near field below threshold [13,14,16]. In the long time limit the near-field intensity and amplitude are both uniform in space on average and only the far field and the correlation function reveal the hidden spatial pattern, a phenomenon that we label either “quantum image” or “quantum pattern.”

It is interesting to ask what one would measure by sampling the output of the OPO with a detector which is fast enough to resolve the quantum fluctuations responsible for the quantum pattern. To answer this question we transform the quantum equations of motion into a set of coupled classical-looking Langevin equations. We then implement numerical codes to integrate the resulting stochastic partial differential equations where quantum fluctuations are simulated by random number generators. In this way we have been able to explore regimes where analytical calculations are not possible, such as for input beams of finite diameter.

This paper is organized as follows. In Sec. II we derive the Langevin equations of motion from the quantum Hamiltonian. Special care is taken to treat the functional derivatives which appear when extending known theories to the spatiotemporal domain. In Sec. III we describe the numerical method for the integration of the (Langevin) stochastic partial differential equations. Section IV is devoted to study the quantum pattern generated by an OPO below threshold with plane mirrors and a homogeneous input beam. We successfully compare correlation functions in the far and near fields obtained by numerical and analytical methods. We show that the far-field intensity of the signal fluctuations has a circular shape that anticipates the incoming pattern above threshold.

*Also at Department of Physics and Applied Physics, University of Strathclyde, Glasgow, Scotland, United Kingdom.

[†]Electronic address: gianluca@phys.strath.ac.uk

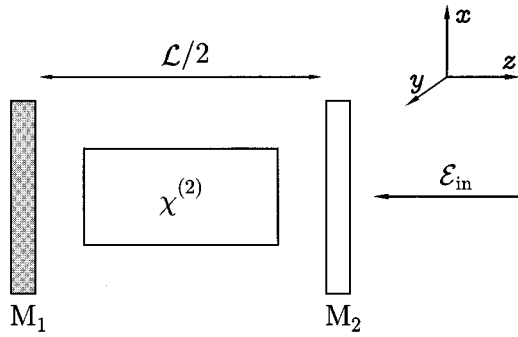


FIG. 1. Experimental setup: a cavity with a $\chi^{(2)}$ medium inside is pumped with a plane-wave input of frequency $2\omega_s$. The nonlinear optical medium generates an output field of frequency ω_s .

Far-field images of the signal fluctuations are by far easier to realize experimentally than quantum correlations in the near field. Moreover, numerical and analytical calculations show that opposite positions along the far-field circle are correlated, i.e., the instantaneous signal field is formed by two off-axis emissions. This information is provided by spatial correlation functions, which, as usual, convey more information than the average distribution. We also show that close to threshold the near-field quantum pattern is surprisingly stable and has a long time scale compared to the inverse decay rate of the resonator. This critical slowing down should make it easier to observe the pattern in an experiment. Section V presents the extension of the numerical simulations to regimes where no analytical calculations are available. In particular we show that quantum images (at least in the correlations and far-field distributions) survive in the case of input pumps with a more realistic, finite Gaussian shape. Finally, Sec. VI contains the generalization to the case of spherical mirrors and homogeneous input beams and conclusions are presented in Sec. VII.

II. LANGEVIN EQUATIONS FOR AN OPO WITH TRANSVERSE EFFECTS

We consider a planar cavity of length $L/2$ (see Fig. 1), where the mirror M_1 is fully reflecting, whereas M_2 has a high, but finite reflectivity. This cavity is pumped with a coherent stationary field with a fixed distribution in the transverse plane, amplitude $\mathcal{E}_{\text{in}}(\vec{x})$ and frequency $2\omega_s$. Inside the cavity, a $\chi^{(2)}$ -nonlinear crystal converts photons of frequency $2\omega_s$ into photons at frequency ω_s and vice versa.

This cavity supports a discrete set of longitudinal modes and a continuous set of transverse modes. We consider the approximation in which only two longitudinal cavity modes are relevant: the pump mode with frequency ω_0 , the closest to the fundamental frequency $2\omega_s$ and the signal mode with frequency ω_1 , the closest to the subharmonic frequency ω_s . We denote by $A_0(\vec{x}, t)$ and $A_1(\vec{x}, t)$ the intracavity field envelope operators of the pump and signal modes, respectively, where $\vec{x} = (x, y)$ spans the plane perpendicular to the direction of light propagation. The inclusion of this degree of freedom allows for an arbitrary field configuration in the transverse plane. The field creation and annihilation operators obey standard equal-time commutation relations

$$[A_i(\vec{x}, t), A_j^\dagger(\vec{x}', t)] = \delta_{ij} \delta(\vec{x} - \vec{x}'), \quad i, j = 0, 1. \quad (1)$$

Hence, $\langle A_j^\dagger(\vec{x}, t) A_j(\vec{x}, t) \rangle$ is the average intensity per unit area of the two fields inside the cavity.

The quantum dynamics for these two fields is described by an extension of the original model [20] to include diffractive effects and has already been presented in [14, 16]. In these papers a master equation was derived from the Hamiltonian of the OPO by expanding the fields over an infinite set of Fourier modes. Here, we rewrite the master equation without the expansion in transverse modes, derive a suitable Fokker-Planck equation for the Wigner probability distribution and obtain appropriate Langevin equations for the dynamics of the fluctuations about the average values of the fields. Particular care is needed when generalizing this standard procedure [21–23] to deal with operators having dependence on the transverse vector \vec{x} . For this reason, we present the most important steps in the derivation of the Langevin equations.

We start from the Hamiltonian which describes the signal and pump dynamics in the interaction picture [14]

$$H = H_f + H_{\text{int}} + H_{\text{ext}} \quad (2)$$

where H_f is the free evolution Hamiltonian given in the paraxial approximation by

$$H_f = \hbar \int d^2\vec{x} A_0^\dagger(\vec{x}, t) \left(\omega_0 - 2\omega_s - \frac{c^2}{4\omega_s} \nabla^2 \right) A_0(\vec{x}, t) + \hbar \int d^2\vec{x} A_1^\dagger(\vec{x}, t) \left(\omega_1 - \omega_s - \frac{c^2}{2\omega_s} \nabla^2 \right) A_1(\vec{x}, t), \quad (3)$$

where

$$\nabla^2 = \frac{\partial^2}{\partial x^2} + \frac{\partial^2}{\partial y^2} \quad (4)$$

is the two-dimensional transverse Laplacian which models the effect of diffraction, H_{int} represents the nonlinear interaction Hamiltonian

$$H_{\text{int}} = \frac{i\hbar g}{2} \int d^2\vec{x} [A_0(\vec{x}, t) (A_1^\dagger(\vec{x}, t))^2 - A_0^\dagger(\vec{x}, t) A_1^2(\vec{x}, t)], \quad (5)$$

g being the nonlinear coupling coefficient, and H_{ext} the term due to the external driving

$$H_{\text{ext}} = i\hbar \int d^2\vec{x} [\mathcal{E}_{\text{in}}(\vec{x}) A_0^\dagger(\vec{x}, t) - \mathcal{E}_{\text{in}}^*(\vec{x}) A_0(\vec{x}, t)]. \quad (6)$$

The Hamiltonian H affects the coherent part of the master equation for the density matrix ρ given by

$$\frac{\partial}{\partial t} \rho = \frac{1}{i\hbar} [H, \rho] + \Lambda \rho, \quad (7)$$

where the latter part of the equation represents the damping due to the finite reflectivity of mirror M_1 and is given by the Liouvillian terms

$$\begin{aligned} \Lambda\rho = & \int d^2\vec{x} \Gamma_0(\vec{x}) [2A_0(\vec{x},t)\rho A_0^\dagger(\vec{x},t) - \rho A_0^\dagger(\vec{x},t)A_0(\vec{x},t) \\ & - A_0^\dagger(\vec{x},t)A_0(\vec{x},t)\rho] + \int d^2\vec{x} \Gamma_1(\vec{x}) [2A_1(\vec{x},t)\rho A_1^\dagger(\vec{x},t) \\ & - \rho A_1^\dagger(\vec{x},t)A_1(\vec{x},t) - A_1^\dagger(\vec{x},t)A_1(\vec{x},t)\rho], \end{aligned} \quad (8)$$

where $\Gamma_i(\vec{x})$ are the space-dependent losses for the two fields.

In order to obtain Langevin equations from the master equation (7), we need to describe the evolution of the appropriate quantum probability distributions. To this end it is convenient to introduce the characteristic functional

$$\begin{aligned} \chi(\{\zeta_i, \zeta_i^*\}, s) = & \text{Tr} \left\{ \rho \exp \left[\int d^2\vec{x} \sum_{i=0,1} (\zeta_i(\vec{x}) A_i^\dagger(\vec{x}) - \zeta_i^*(\vec{x}) \right. \right. \\ & \left. \left. \times A_i(\vec{x})) \right] \exp \left[\frac{s}{2} \int d^2\vec{x} \sum_{i=0,1} |\zeta_i(\vec{x})|^2 \right] \right\}. \end{aligned} \quad (9)$$

Note that the dependence from the time t has been omitted in order to lighten the notation. In the definition (9), $\zeta_i(\vec{x})$ are the Fourier conjugates of the c -number fields $\alpha_i(\vec{x})$ associated with the operators $A_i(\vec{x})$, while the variable s is related to either the Glauber-Sudarshan (P) distribution ($s=+1$), or the Wigner (W) distribution ($s=0$), or the Q distribution ($s=-1$) [24]. In order to make the notation compact, we express these three distributions in the form

$$\begin{aligned} W(\{\alpha_i, \alpha_i^*\}, s) = & \int \mathcal{D}\zeta_0 \mathcal{D}\zeta_0^* \mathcal{D}\zeta_1 \mathcal{D}\zeta_1^* \chi(\{\zeta_i, \zeta_i^*\}, s) \\ & \times \exp \left[\int d^2\vec{x} \sum_{i=0,1} (\alpha_i(\vec{x}) \zeta_i^*(\vec{x}) \right. \\ & \left. - \alpha_i^*(\vec{x}) \zeta_i(\vec{x})) \right], \end{aligned} \quad (10)$$

where $\int \mathcal{D}\zeta_0 \cdots \mathcal{D}\zeta_1^*$ indicates *functional* integration with respect to the functions $\zeta_0 \cdots \zeta_1^*$ [25]. The normalization of functional integrals is a notoriously difficult problem [25]. Thankfully, only the functional form of $W(\{\alpha_i, \alpha_i^*\}, s)$ is relevant here so that issues of normalization need not to concern us. The equation of motion for the distribution functionals (10) is obtained from the master equation via the formal substitution of the terms involving the density matrix ρ with suitable operations over the distribution functionals. It is easy to see, for example, that

$$\begin{aligned} \rho A_i^\dagger(\vec{x}) \Leftrightarrow & \left[\alpha_i^*(\vec{x}) + \frac{1-s}{2} \frac{\delta}{\delta \alpha_i(\vec{x})} \right] W(\{\alpha_i, \alpha_i^*\}, s), \\ A_i^\dagger(\vec{x}) \rho \Leftrightarrow & \left[\alpha_i^*(\vec{x}) - \frac{1+s}{2} \frac{\delta}{\delta \alpha_i(\vec{x})} \right] W(\{\alpha_i, \alpha_i^*\}, s), \end{aligned} \quad (11)$$

$$\rho A_i(\vec{x}) \Leftrightarrow \left[\alpha_i(\vec{x}) - \frac{1+s}{2} \frac{\delta}{\delta \alpha_i^*(\vec{x})} \right] W(\{\alpha_i, \alpha_i^*\}, s),$$

$$A_i(\vec{x}) \rho \Leftrightarrow \left[\alpha_i(\vec{x}) + \frac{1-s}{2} \frac{\delta}{\delta \alpha_i^*(\vec{x})} \right] W(\{\alpha_i, \alpha_i^*\}, s),$$

where we have introduced the *functional* derivatives $\delta W(\{\alpha_i, \alpha_i^*\}, s) / \delta \alpha_i(\vec{x})$ [26]. Functional differentiation has been applied in quantum optics to generalized operator ordering theorems to continuum operators [27].

Equations (11) are sufficient, for example, to determine all the terms of the evolution equation for the distributions (10) coming from the Liouvillian terms (8) of the master equation. The only terms of Eq. (7) that require special attention, are the diffraction terms which appear in the free Hamiltonian H_f of Eq. (3). As one obtains after some algebraic manipulations, such terms have the form

$$\begin{aligned} 2^i \frac{ic^2}{4\omega_s} \int d^2\vec{x} \frac{1}{2} \left\{ \left[\nabla^2 \alpha_i^*(\vec{x}), \frac{\delta}{\delta \alpha_i^*(\vec{x})} \right]_+ \right. \\ \left. - \left[\nabla^2 \alpha_i(\vec{x}), \frac{\delta}{\delta \alpha_i(\vec{x})} \right]_+ - s \left[\nabla^2 \alpha_i^*(\vec{x}), \frac{\delta}{\delta \alpha_i^*(\vec{x})} \right] \right. \\ \left. + s \left[\nabla^2 \alpha_i(\vec{x}), \frac{\delta}{\delta \alpha_i(\vec{x})} \right] \right\} W(\{\alpha_i, \alpha_i^*\}, s), \quad i=0,1, \end{aligned} \quad (12)$$

where $[\cdot, \cdot]_+$ is the anticommutator and, in deriving Eq. (12), we made use of the integration by parts

$$\int d^2\vec{x} \alpha_i(\vec{x}) \nabla^2 \frac{\delta}{\delta \alpha_i(\vec{x})} = \int d^2\vec{x} (\nabla^2 \alpha_i(\vec{x})) \frac{\delta}{\delta \alpha_i(\vec{x})}. \quad (13)$$

It follows from the definition of functional differentiation [25] that

$$\left[\frac{\delta}{\delta \alpha_i(\vec{x})}, \alpha_i(\vec{x}') \right] = \left[\frac{\delta}{\delta \alpha_i^*(\vec{x})}, \alpha_i^*(\vec{x}') \right] = \delta(\vec{x}' - \vec{x}), \quad (14)$$

where functional derivatives are understood to act under an integral. The diffraction terms (12) can now be recasted as

$$\begin{aligned} 2^i \frac{ic^2}{4\omega_s} \int d^2\vec{x} \left\{ \frac{\delta}{\delta \alpha_i^*(\vec{x})} [\nabla^2 \alpha_i^*(\vec{x})] \frac{\delta}{\delta \alpha_i(\vec{x})} [\nabla^2 \alpha_i(\vec{x})] \right\} \\ \times W(\{\alpha_i, \alpha_i^*\}, s). \end{aligned} \quad (15)$$

Finally, we are ready to obtain the equation of motion for the probability distributions $W(\{\alpha_i, \alpha_i^*\}, s)$. Since we are interested here in the dynamics of quantum fluctuations [28] around the semiclassical mean value, we consider the c -number fields $\Delta\alpha_i$ defined as

$$\Delta\alpha_0(\vec{x}) = \alpha_0(\vec{x}) - \mathcal{A}_0(\vec{x}), \quad \Delta\alpha_1(\vec{x}) = \alpha_1(\vec{x}) - \mathcal{A}_1(\vec{x}), \quad (16)$$

where $\mathcal{A}_i(\vec{x})$ are the semiclassical mean values of the pump ($i=0$) and signal ($i=1$) fields, respectively. Using a standard linearization procedure (see, e.g., [22]), the equation of motion for the distribution functional $W(\{\Delta\alpha_i, \Delta\alpha_i^*\}, s)$ is expanded in a power series of the inverse of an appropriate system size parameter, and one can obtain at once the macroscopic law of motion describing the evolution of the semiclassical fields [17]

$$\begin{aligned} \frac{\partial}{\partial t} \mathcal{A}_0(\vec{x}) &= - \left(\Gamma_0(\vec{x}) + i\omega_0 - 2i\omega_s - i \frac{c^2}{4\omega_s} \nabla^2 \right) \mathcal{A}_0(\vec{x}) \\ &\quad - \frac{g}{2} \mathcal{A}_1^2(\vec{x}) + \mathcal{E}_{\text{in}}(\vec{x}), \\ \frac{\partial}{\partial t} \mathcal{A}_1(\vec{x}) &= - \left(\Gamma_1(\vec{x}) + i\omega_1 - i\omega_s - i \frac{c^2}{2\omega_s} \nabla^2 \right) \mathcal{A}_1(\vec{x}) \\ &\quad + g \mathcal{A}_0(\vec{x}) \mathcal{A}_1^*(\vec{x}), \end{aligned} \quad (17)$$

and the linearized Fokker-Planck equation, which describes the dynamics of quantum fluctuations in the limit of large system size

$$\begin{aligned} &\frac{\partial W(\{\Delta\alpha_i, \Delta\alpha_i^*\}, s)}{\partial t} \\ &= \left\{ \int d^2\vec{x} \sum_{j=0,1} \left[\left(- \frac{\delta}{\delta\Delta\alpha_j(\vec{x})} \mathcal{Q}_j(\Delta\alpha_i(\vec{x})) + \text{c.c.} \right) \right. \right. \\ &\quad \left. \left. + \frac{1}{2} \int d^2\vec{x}' \frac{\delta^2}{\delta\Delta\alpha_j^\mu(\vec{x}) \delta\Delta\alpha_j^\nu(\vec{x}')} D_j^{\mu,\nu}(\vec{x}, \vec{x}') \right] \right\} \\ &\quad \times W(\{\Delta\alpha_i, \Delta\alpha_i^*\}, s), \end{aligned} \quad (18)$$

where $\mathcal{Q}_j(\Delta\alpha_i(\vec{x}))$ are the drift terms

$$\begin{aligned} \mathcal{Q}_0(\Delta\alpha_i(\vec{x})) &= - \left(\Gamma_0(\vec{x}) + i\omega_0 - 2i\omega_s - i \frac{c^2}{4\omega_s} \nabla^2 \right) \Delta\alpha_0(\vec{x}) \\ &\quad - g \mathcal{A}_1(\vec{x}) \Delta\alpha_1(\vec{x}), \\ \mathcal{Q}_1(\Delta\alpha_i(\vec{x})) &= - \left(\Gamma_1(\vec{x}) + i\omega_1 - i\omega_s - i \frac{c^2}{2\omega_s} \nabla^2 \right) \Delta\alpha_1(\vec{x}) \\ &\quad + g \mathcal{A}_0(\vec{x}) \Delta\alpha_1^*(\vec{x}) + g \mathcal{A}_1^*(\vec{x}) \Delta\alpha_0(\vec{x}), \end{aligned} \quad (19)$$

and $D_j^{\mu,\nu}(\vec{x}, \vec{x}')$ are generalized diffusion matrices such that $\mu, \nu=1$ and $\mu, \nu=2$ correspond to $\Delta\alpha_j(\vec{x})$ and to $\Delta\alpha_j^*(\vec{x})$, respectively. The nonzero elements of these diffusion matrices are

$$\begin{aligned} D_1^{1,1}(\vec{x}, \vec{x}') &= -g s \mathcal{A}_0(\vec{x}) \delta(\vec{x} - \vec{x}'), \\ D_1^{2,2}(\vec{x}, \vec{x}') &= -g s \mathcal{A}_0^*(\vec{x}) \delta(\vec{x} - \vec{x}'), \end{aligned} \quad (20)$$

$$D_j^{1,2}(\vec{x}, \vec{x}') = D_j^{2,1}(\vec{x}, \vec{x}') = \Gamma_j(\vec{x}) (1+s) \delta(\vec{x} - \vec{x}'), \quad j=0,1.$$

At the present stage we neglect the effects of third-order nonlinearities, an approximation which is valid in the limit of small quantum noise, i.e., for a macroscopic system not too close to critical points.

In the Wigner representation (i.e., for $s=0$) the diffusion matrices (20) are positive definite; hence, the equation of motion (18) for the Wigner functional can be interpreted in terms of a classical stochastic process which obeys Ito stochastic differential equations of the type [21]

$$d\Delta\alpha_j(\vec{x}) = \mathcal{Q}_j(\Delta\alpha_i(\vec{x})) dt + dB_j^1(\vec{x}), \quad (21)$$

where dB_j^μ are Wiener increments, such that $\langle dB_j^\mu(\vec{x}) dB_i^\nu(\vec{x}') \rangle = \delta_{i,j} D_j^{\mu,\nu}(\vec{x}, \vec{x}') dt$.

We provide here the explicit expression of Eq. (21) in the form of a classical-looking set of Langevin equations of motion for the fluctuations $\Delta\alpha_0(\vec{x})$ and $\Delta\alpha_1(\vec{x})$ of the pump and signal fields, respectively:

$$\begin{aligned} \frac{\partial}{\partial t} \Delta\alpha_0(\vec{x}) &= - \left(\Gamma_0(\vec{x}) + i\omega_0 - 2i\omega_s - i \frac{c^2}{4\omega_s} \nabla^2 \right) \Delta\alpha_0(\vec{x}) \\ &\quad - g \mathcal{A}_1(\vec{x}) \Delta\alpha_1(\vec{x}) + \sqrt{2\Gamma_0(\vec{x})} \xi_0(\vec{x}, t), \end{aligned} \quad (22)$$

$$\begin{aligned} \frac{\partial}{\partial t} \Delta\alpha_1(\vec{x}) &= - \left(\Gamma_1(\vec{x}) + i\omega_1 - i\omega_s - i \frac{c^2}{2\omega_s} \nabla^2 \right) \Delta\alpha_1(\vec{x}) \\ &\quad + g \mathcal{A}_0(\vec{x}) \Delta\alpha_1^*(\vec{x}) + g \mathcal{A}_1^*(\vec{x}) \Delta\alpha_0(\vec{x}) \\ &\quad + \sqrt{2\Gamma_1(\vec{x})} \xi_1(\vec{x}, t), \end{aligned} \quad (23)$$

where the Langevin force terms $\xi_i(\vec{x}, t)$ are described by stationary, Gaussian, stochastic processes with zero average and correlation functions given by

$$\begin{aligned} \langle \xi_i^*(\vec{x}, t) \xi_j(\vec{x}', t') \rangle &= \frac{1}{2} \delta(\vec{x} - \vec{x}') \delta(t - t') \delta_{i,j}, \\ \langle \xi_i(\vec{x}, t) \xi_j(\vec{x}', t') \rangle &= 0. \end{aligned} \quad (24)$$

The noise terms in Eqs. (22) and (23) can be interpreted as the vacuum quantum noise entering through the partially transmitting mirror M_1 .

Quantities $\mathcal{A}_i(\vec{x})$ in Eqs. (22) and (23) are the stationary semiclassical mean values of the OPO fields which are obtained by the integration of the semiclassical equations (17).

Equations (22) and (23) are stochastic partial differential equations with space-dependent coefficients; they represent the main topic of our analysis. They can be used both above and below the signal threshold and treating them requires sophisticated numerical methods. In the following we concentrate our analysis on the behavior of quantum fluctuations below the OPO threshold. In this case the expectation value of the signal field is identically zero, so that the fluctuations of the signal field coincide with the signal field itself and Eq. (23) decouples from Eq. (22). (Note that below threshold the linearization procedure outlined above corresponds to neglecting the pump depletion.)

III. NUMERICAL INTEGRATION OF THE LANGEVIN EQUATIONS

The numerical integration of the Langevin equations (22) and (23) requires the discretization of both space and time. We solve the equations in a square of side b in the transverse plane, with periodic boundary conditions and we use a spatial grid of $N \times N$ points with N ranging from 64 up to 256. A discrete version of the OPO fields and of the Langevin forces is introduced as

$$\Delta \tilde{\alpha}_j^{nm}(t) = \frac{1}{\mathcal{F}_{nm}} \int_{\mathcal{F}_{nm}} d^2 \vec{x} \Delta \alpha_j(\vec{x}, t), \quad j=0,1, \quad (25)$$

$$\tilde{\xi}_j^{nm}(t) = \frac{1}{\mathcal{F}_{nm}} \int_{\mathcal{F}_{nm}} d^2 \vec{x} \sqrt{2\Gamma_j(\vec{x})} \xi_j(\vec{x}, t), \quad j=0,1, \quad (26)$$

where the indexes n, m identify the grid point and $\mathcal{F}_{nm} = (\Delta x)^2$ are sufficiently small and disjunct areas covering the transverse plane. The diffractive terms of the Langevin equations (22) and (23) can easily be handled by using a split-step technique with high spatial accuracy [29] or even a simple-minded Euler discretization scheme in the case of plane mirrors, uniform losses, flat pumps, and OPO's below threshold.

In order to discuss the numerical method used for the temporal discretization of the OPO Langevin equations, it is useful to introduce a $4 \times N \times N$ vector \mathbf{X} , containing the discretized OPO fields $\Delta \alpha_0^{nm} (\Delta \alpha_0^{nm})^* \Delta \alpha_1^{nm} (\Delta \alpha_1^{nm})^*$ (ordering of the vector elements is not important here) and a $4 \times N \times N$ vector Θ containing the discretized Langevin forces. Equations (22) and (23) can then be recasted in a compact matricial form:

$$\frac{d}{dt} \mathbf{X}(t) = \mathbf{L}_{\text{det}} \mathbf{X}(t) + \Theta(t) \quad (27)$$

where \mathbf{L}_{det} is a deterministic operator (containing the diffraction). A formal solution of Eq. (27) during a time step Δt of the numerical integration is given by

$$\begin{aligned} \mathbf{X}(t + \Delta t) &= \exp[\mathbf{L}_{\text{det}} \Delta t] \mathbf{X}(t) + \int_t^{t+\Delta t} dt' \\ &\quad \times \exp[\mathbf{L}_{\text{det}}(t + \Delta t - t')] \Theta(t'). \end{aligned} \quad (28)$$

The simplest approximation to the stochastic integral on the right-hand side (RHS) consists in replacing the exponential operator inside the integral by an identity: it is easy to see that this approximation leads to an error in the calculation of the second-order field correlations which goes to zero as the time interval Δt . On the other side it can be shown that the approximation

$$\begin{aligned} &\int_t^{t+\Delta t} dt' \exp[\mathbf{L}_{\text{det}}(t + \Delta t - t')] \Theta(t') \\ &\approx \exp\left[\mathbf{L}_{\text{det}} \frac{\Delta t}{2}\right] \int_t^{t+\Delta t} dt' \Theta(t') \end{aligned} \quad (29)$$

affects the evaluation of the correlation function of fluctuating fields with an error which goes to zero as Δt^2 . The inte-

gral in the RHS of Eq. (29) is by definition of Langevin forces a vector of Gaussian stochastic variables with a variance $\propto \Delta t$. By combining Eqs. (28) and (29) we can write

$$\begin{aligned} \mathbf{X}(t + \Delta t) &\approx \exp\left[\mathbf{L}_{\text{det}} \frac{\Delta t}{2}\right] \left(\exp\left[\mathbf{L}_{\text{det}} \frac{\Delta t}{2}\right] \mathbf{X}(t) \right. \\ &\quad \left. + \int_t^{t+\Delta t} dt' \Theta(t') \right). \end{aligned} \quad (30)$$

This formula leads to a simple integration algorithm: at each time step let the fields evolve for half a step with the deterministic operator alone, then add random Gaussian noise terms in each space point, then make another half step of deterministic evolution. (As one can easily verify, the half steps are actually performed only at the begin and end of the time evolution). The validity of this approximation is demonstrated in the Appendix. Even in the presence of a numerical integrator of a second-order accuracy in time, particular care needs to be taken when selecting the time step Δt . Convergence of the numerical codes requires time steps smaller than for the integration of nonstochastic partial differential equations.

IV. OPO CAVITY WITH PLANE MIRRORS AND A HOMOGENEOUS INPUT BEAM

A first test of the Langevin model (22) and (23) is represented by the case of plane mirrors, flat losses [i.e., $\Gamma_i(\vec{x}) = \gamma_i$], and a homogeneous input beam [i.e., $\mathcal{E}_{\text{in}}(\vec{x}) = E$ assumed here to be real]. Analytic evaluations of the correlation functions [14], far-field distributions, and squeezing spectra are available [13] and make it possible to check the accuracy of the numerical integration of the stochastic partial differential equations (22) and (23). Below threshold, these Langevin equations decouple and we focus our attention on the dynamics of the signal fluctuations. It is then convenient to introduce the following time and space normalizations:

$$\tau = \gamma_1 t, \quad \vec{x} = \frac{\vec{x}}{\sqrt{a}}, \quad (31)$$

with

$$a = c / (2\omega_s \gamma_1), \quad (32)$$

which transform Eq. (23) into

$$\begin{aligned} \frac{\partial}{\partial \tau} \Delta \tilde{\alpha}_1(\vec{x}, \tau) &= -(1 + i\delta_1 - i\nabla^2) \Delta \tilde{\alpha}_1(\vec{x}, \tau) \\ &\quad + \tilde{\mathcal{A}}_0 \Delta \tilde{\alpha}_1^*(\vec{x}, \tau) + \sqrt{2} \tilde{\xi}_1(\vec{x}, \tau), \end{aligned} \quad (33)$$

where we have defined the signal detuning and normalized the average pump field and the fluctuations via

$$\begin{aligned} \delta_1 &\equiv \frac{\omega_1 - \omega_s}{\gamma_1}, \\ \tilde{\mathcal{A}}_0 &= \frac{g}{\gamma_1} \mathcal{A}_0, \\ \Delta \tilde{\alpha}_1 &= \Delta \alpha_1 \sqrt{a}, \quad \tilde{\xi}_1(\vec{x}, \tau) = \sqrt{\frac{a}{\gamma_1}} \xi_1(\vec{x}, \tau), \end{aligned} \quad (34)$$

so that we have the correlation function

$$\langle \tilde{\xi}_1^*(\vec{x}, \tau) \tilde{\xi}_1(\vec{x}', \tau') \rangle = \frac{1}{2} \delta(\vec{x} - \vec{x}') \delta(\tau - \tau'). \quad (35)$$

We begin by noting that below threshold the dynamics of the semiclassical equations (17) relaxes to the homogeneous state given by

$$\tilde{\mathcal{A}}_0 = \frac{g \mathcal{E}_{\text{in}}}{\gamma_1 [\gamma_0 + i(\omega_0 - 2\omega_s)]}, \quad \mathcal{A}_1 = 0. \quad (36)$$

By increasing the input intensity, a second-order phase transition corresponding to the loss of stability of Eq. (36) and the generation of a signal field occurs. In Ref. [17] it was shown that diffraction lowers the threshold intensity and that the character of the solution above threshold depends on the sign of the signal detuning δ_1 . In particular it was demonstrated that [17] (i) if $\delta_1 > 0$, the trivial solution (36) becomes unstable with respect to the onset of a uniform signal wave propagating along the longitudinal axis when the pump field intensity $|\tilde{\mathcal{A}}_0|^2$ reaches the value $(1 + \delta_1^2)^2$. The output signal is homogeneous in space because the most unstable mode corresponds to a wave vector \vec{k} with $k=0$; (ii) for negative signal detunings δ_1 the most unstable mode corresponds to a wave vector of magnitude equal to

$$k_{\text{crit}} = \sqrt{-\delta_1}. \quad (37)$$

The threshold for this transition is $|\tilde{\mathcal{A}}_0| = 1$ and thus lower than for positive detunings. Above threshold there is the spontaneous formation of a roll (or stripe) pattern with a separation between rolls equal to $2\pi/k_{\text{crit}}$.

As already hinted above, it is possible to find for the case analyzed in this section analytical expressions for the squeezing spectra and near-field correlations of the signal fluctuations [13,14]. Here we follow an alternative approach based on the Langevin equation (33) and the analytical evaluation of correlation functions in the Fourier domain (far field).

A. Far-field correlation functions

As it is well known, the far field corresponds to the Fourier transform of the near field. In the ideal case of an infinite transverse plane and a plane wave input field, as we consider here, the far field is located at an infinite distance from the cavity mirrors. However, it can be carried to a finite distance by placing a lens at a distance from the cavity equal to its focal length. Of course, the presence of the lens breaks the translational symmetry and introduces an axis for the system.

Equation (33) is a linear stochastic partial differential equation which allows analytical solutions for the correlation functions in the Fourier domain. By dropping unessential tildes and by introducing

$$\beta(\vec{k}, \tau) = \frac{1}{2\pi} \int d^2\vec{x} \Delta \alpha_1(\vec{x}, \tau) \exp(i\vec{k} \cdot \vec{x}) \quad (38)$$

with \vec{k} being the transverse wave vector $\vec{k} = (k_x, k_y)$, Eq. (33) and its complex conjugate are rewritten in a convenient matrix form as

$$\begin{aligned} \frac{\partial}{\partial \tau} \begin{pmatrix} \beta(\vec{k}, \tau) \\ \beta^*(-\vec{k}, \tau) \end{pmatrix} &= \begin{pmatrix} -(1+i\sigma_k) & \mathcal{A}_0 \\ \mathcal{A}_0^* & -(1-i\sigma_k) \end{pmatrix} \\ &\times \begin{pmatrix} \beta(\vec{k}, \tau) \\ \beta^*(-\vec{k}, \tau) \end{pmatrix} + \sqrt{2} \begin{pmatrix} \eta(\vec{k}, \tau) \\ \eta^*(-\vec{k}, \tau) \end{pmatrix}, \end{aligned} \quad (39)$$

where the Fourier components of the Langevin forces satisfy

$$\langle \eta^*(\vec{k}, \tau) \eta(\vec{k}', \tau') \rangle = \frac{1}{2} \delta(\vec{k} - \vec{k}') \delta(\tau - \tau'),$$

$$\langle \eta(\vec{k}, \tau) \eta(\vec{k}', \tau') \rangle = 0, \quad (40)$$

and where we have introduced the wave-vector-dependent detuning

$$\sigma_k = \delta_1 + k^2. \quad (41)$$

Equations (39) describe the stochastic dynamics of the field fluctuations in the far field. The formal solution of Eq. (39) is given by

$$\begin{aligned} \begin{pmatrix} \beta(\vec{k}, \tau) \\ \beta^*(-\vec{k}, \tau) \end{pmatrix} &= e^{M\tau} \begin{pmatrix} \beta(\vec{k}, 0) \\ \beta^*(-\vec{k}, 0) \end{pmatrix} \\ &+ \sqrt{2} e^{M\tau} \int_0^\tau d\tau' e^{-M\tau'} \begin{pmatrix} \eta(\vec{k}, \tau') \\ \eta^*(-\vec{k}, \tau') \end{pmatrix}, \end{aligned} \quad (42)$$

where M is the 2×2 matrix appearing in Eq. (39). By using Eq. (42) it is straightforward to show that

$$\begin{aligned} \langle \beta(\vec{k}, \tau) \eta^*(\vec{k}', \tau) \rangle &= \sqrt{2} e^{M\tau} \int_0^\tau d\tau' e^{-M\tau'} \\ &\times \langle \eta(\vec{k}, \tau') \eta^*(\vec{k}', \tau) \rangle \\ &= \frac{1}{2\sqrt{2}} \delta(\vec{k} - \vec{k}'), \\ \langle \beta(\vec{k}, \tau) \eta(\vec{k}', \tau) \rangle &= 0, \end{aligned} \quad (43)$$

where a factor 1/2 arises due to the δ -function on time being located at the upper limit of integration.

We are interested in the evolution of the correlation functions $\langle \beta(\vec{k}, \tau) \beta(\vec{k}', \tau) \rangle$ and $\langle \beta(\vec{k}, \tau) \beta^*(-\vec{k}', \tau) \rangle$. Their equations of motion are readily obtained from Eqs. (39) and (43):

$$\begin{aligned} \frac{\partial}{\partial \tau} \langle \beta(\vec{k}, \tau) \beta(\vec{k}', \tau) \rangle &= -[2 + i(\sigma_k + \sigma_{k'})] \langle \beta(\vec{k}, \tau) \beta(\vec{k}', \tau) \rangle \\ &+ \mathcal{A}_0 \langle \beta^*(-\vec{k}, \tau) \beta(\vec{k}', \tau) \rangle \\ &+ \langle \beta(\vec{k}, \tau) \beta^*(-\vec{k}', \tau) \rangle, \end{aligned} \quad (44)$$

$$\begin{aligned}
\frac{\partial}{\partial \tau} \langle \beta(\vec{k}, \tau) \beta^*(-\vec{k}', \tau) \rangle &= -[2 + i(\sigma_k - \sigma_{k'})] \\
&\times \langle \beta(\vec{k}, \tau) \beta^*(-\vec{k}', \tau) \rangle \\
&+ \mathcal{A}_0 \langle \beta^*(-\vec{k}, \tau) \beta^*(-\vec{k}', \tau) \rangle \\
&+ \mathcal{A}_0^* \langle \beta(\vec{k}, \tau) \beta(\vec{k}', \tau) \rangle + \delta(\vec{k} + \vec{k}').
\end{aligned} \tag{45}$$

The dynamics (44) and (45) of the correlation functions of interest is nothing but a relaxation, after a suitable transient, to stationary values. Such stationary values are obtained by solving an algebraic system of equations of the form

$$\mathcal{B}\vec{V} = \vec{W}, \tag{46}$$

where the 4×4 matrix \mathcal{B} is given by

$$\mathcal{B} = \begin{pmatrix} -[2 + i(\sigma_k + \sigma_{k'})] & 0 & \mathcal{A}_0 & \mathcal{A}_0 \\ 0 & -[2 - i(\sigma_k + \sigma_{k'})] & \mathcal{A}_0^* & \mathcal{A}_0^* \\ \mathcal{A}_0^* & \mathcal{A}_0 & -[2 + i(\sigma_k - \sigma_{k'})] & 0 \\ \mathcal{A}_0^* & \mathcal{A}_0 & 0 & -[2 - i(\sigma_k - \sigma_{k'})] \end{pmatrix} \tag{47}$$

and where the vectors \vec{V} and \vec{W} are

$$\vec{V} = \begin{pmatrix} \langle \beta(\vec{k}) \beta(\vec{k}') \rangle \\ \langle \beta^*(-\vec{k}) \beta^*(-\vec{k}') \rangle \\ \langle \beta(\vec{k}) \beta^*(-\vec{k}') \rangle \\ \langle \beta^*(-\vec{k}) \beta(\vec{k}') \rangle \end{pmatrix}, \quad \vec{W} = \delta(\vec{k} + \vec{k}') \begin{pmatrix} 0 \\ 0 \\ -1 \\ -1 \end{pmatrix}, \tag{48}$$

respectively. Simple algebra then leads to the expressions

$$\begin{aligned}
\langle \beta(\vec{k}) \beta(\vec{k}') \rangle &= \frac{4\mathcal{A}_0[2 - i(\sigma_k + \sigma_{k'})]}{[4 + (\sigma_k + \sigma_{k'})^2][4 + (\sigma_k - \sigma_{k'})^2] - 16|\mathcal{A}_0|^2} \\
&\times \delta(\vec{k} + \vec{k}'),
\end{aligned} \tag{49}$$

$$\begin{aligned}
\langle \beta(\vec{k}) \beta^*(-\vec{k}') \rangle &= \frac{[4 + (\sigma_k + \sigma_{k'})^2][2 - i(\sigma_k - \sigma_{k'})]}{[4 + (\sigma_k + \sigma_{k'})^2][4 + (\sigma_k - \sigma_{k'})^2] - 16|\mathcal{A}_0|^2} \\
&\times \delta(\vec{k} + \vec{k}').
\end{aligned} \tag{50}$$

Let us remind the reader now that the Wigner representation provides the expectation values of symmetrically ordered quantities. For example,

$$\begin{aligned}
\langle \alpha_1^*(\vec{x}, \tau) \alpha_1(\vec{x}', \tau) \rangle &= \frac{1}{2} [\langle A_1^\dagger(\vec{x}, \tau) A_1(\vec{x}', \tau) \rangle \\
&+ \langle A_1(\vec{x}, \tau) A_1^\dagger(\vec{x}', \tau) \rangle] \\
&= \langle A_1^\dagger(\vec{x}, \tau) A_1(\vec{x}', \tau) \rangle + \frac{1}{2} \delta(\vec{x} - \vec{x}').
\end{aligned} \tag{51}$$

For this reason the mean intensity of the signal far field, which is obtained from the correlation function (50) for $\vec{k}' = -\vec{k}$, is given by

$$\langle \beta(\vec{k}, \tau) \beta^*(\vec{k}, \tau) \rangle - \frac{1}{2} \delta(0) = \frac{1}{2} \frac{|\mathcal{A}_0|^2}{1 + \sigma_k^2 - |\mathcal{A}_0|^2} \delta(0). \tag{52}$$

The presence of the factor $\delta(0)$ must not be seen with alarm. It arises from the fact that in the flat pump model the signal field fluctuations in the transverse plane do not vanish for $|\vec{x}| \rightarrow \infty$ so that their Fourier transforms are singular.

By introducing periodic boundary conditions in a square of side b , we can express, for example, $\Delta \alpha_1$ in the form

$$\Delta \alpha_1(\vec{x}, \tau) = \sum_{\vec{n}} \frac{1}{b} \exp(-i\vec{k}_{\vec{n}} \cdot \vec{x}) f_{\vec{k}_{\vec{n}}}(\tau), \tag{53}$$

$$\vec{k}_{\vec{n}} = \frac{2\pi}{b} \vec{n},$$

$$\vec{n} = (n_x, n_y), \quad n_x, n_y = 0, \pm 1, \pm 2, \dots \tag{54}$$

The far field amplitude of the field fluctuations (38) is related to the coefficients $f_{\vec{k}_{\vec{n}}}$ by

$$\beta(\vec{k}, \tau) = \frac{2\pi}{b} \sum_{\vec{n}} f_{\vec{k}_{\vec{n}}}(\tau) \delta(\vec{k} - \vec{k}_{\vec{n}}). \tag{55}$$

Hence,

$$\beta(\vec{k}, \tau) \beta^*(\vec{k}, \tau) = \left(\frac{2\pi}{b} \right)^2 \sum_{\vec{n}} f_{\vec{k}_{\vec{n}}}(\tau) f_{\vec{k}_{\vec{n}}}^*(\tau) \delta(\vec{k} - \vec{k}_{\vec{n}}) \delta(0) \tag{56}$$

and in the continuum limit $b \rightarrow \infty$, in which $(2\pi/b)^2 \sum_{\vec{n}} \rightarrow \int d^2\vec{k}$, one has

$$\beta(\vec{k}, \tau) \beta^*(\vec{k}, \tau) = f_{\vec{k}}(\tau) f_{\vec{k}}^*(\tau) \delta(0). \tag{57}$$

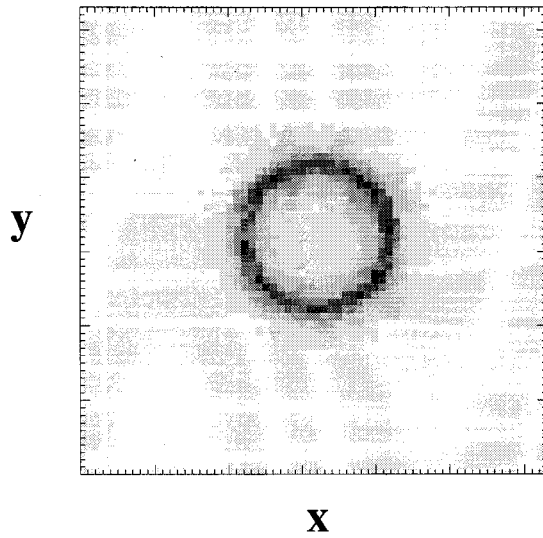


FIG. 2. Time average of the far-field intensity of the signal fluctuations for $\mathcal{A}_0=0.97$ and $\delta_1=-1$. Higher intensities correspond to darker areas.

As in the near field, the mean intensity in the far field (52) is nonzero, but contrary to the near field, it is not uniform. The intensity distribution presents a maximum for $\sigma_k=0$, i.e., for

$$|k|^2 = -\delta_1, \quad (58)$$

which, when $\delta_1 < 0$, is just the magnitude of the wave vector of the pattern above threshold [see Eq. (37)]. Since Eq. (50) depends only on $|k|^2$ we expect the far-field intensity distribution for negative detunings δ_1 to be an annulus centered at the critical circle of radius defined by Eq. (37). This is confirmed by the numerical integration of Eq. (33) as displayed in Fig. 2. In order to provide a better comparison between numerical and analytical data, we present in Fig. 3 the numerical results for the far-field intensity averaged over time and over the azimuthal angle φ which spans the critical circle; they are displayed as a section of the intensity profile along the axis k_x for three values of \mathcal{A}_0 . The corresponding analytical results, given by Eq. (52), are shown in Fig. 3(a). In the numerical simulations, the Dirac δ function has a finite value, due to the finiteness of the spatial grid; in the comparison we have adjusted the arbitrary vertical scale in Fig. 3 in such a way that the maxima of numerical and analytical curves coincide and the agreement turns out to be excellent. As threshold is approached, the peak of the far field intensity increases and the annulus becomes narrower and narrower around the critical radius; these features should be experimentally accessible (of course, the divergence of the peak is an artifact of the linearization around the stationary state).

The homodyne detection of signal photons in the far field corresponds to the measure of two orthogonal quadrature components. By choosing the reference phase in such a way that \mathcal{A}_0 is real, the two significant quadratures are $X(\vec{k}) = \beta(\vec{k}) + \beta^*(\vec{k})$ and $Y(\vec{k}) = -i[\beta(\vec{k}) - \beta^*(\vec{k})]$; by using Eqs. (49) and (50) their correlation function can be calculated as

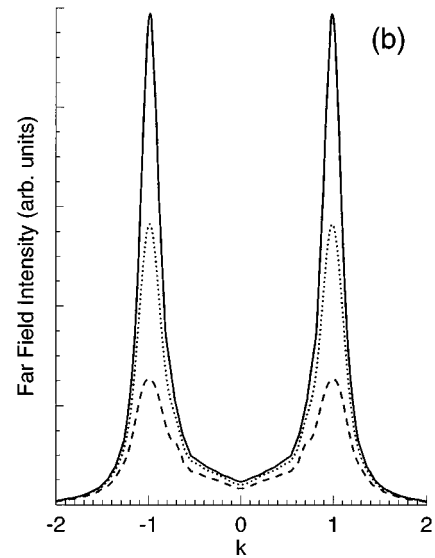
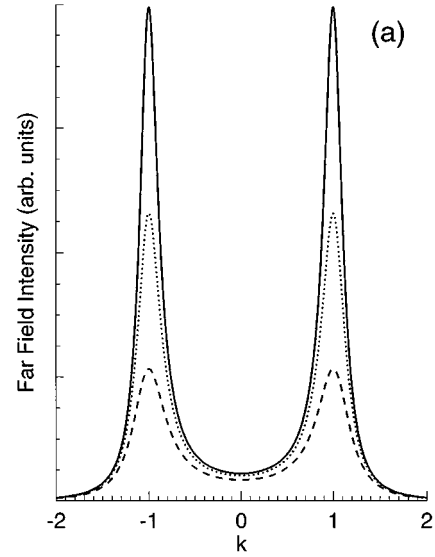


FIG. 3. Comparison between theory (a) and Langevin simulations (b) of the far-field intensity of the signal fluctuations averaged in time and along the polar angle spanning the circle of Fig. 2 for $\delta_1=-1$ and three values of \mathcal{A}_0 : 0.90 (lowest dashed curve), 0.95 (upper dashed curve), and 0.97 (solid line).

$$\begin{aligned} \langle X(\vec{k})X(\vec{k}') \rangle &= \delta(\vec{k}-\vec{k}') + \delta(\vec{k}+\vec{k}') \frac{\mathcal{A}_0^2}{1+\sigma_k^2-\mathcal{A}_0^2} \\ &\quad + \delta(\vec{k}+\vec{k}') \frac{\mathcal{A}_0}{1+\sigma_k^2-\mathcal{A}_0^2}, \end{aligned} \quad (59)$$

$$\begin{aligned} \langle Y(\vec{k})Y(\vec{k}') \rangle &= \delta(\vec{k}-\vec{k}') + \delta(\vec{k}-\vec{k}') \frac{\mathcal{A}_0^2}{1+\sigma_k^2-\mathcal{A}_0^2} \\ &\quad - \delta(\vec{k}+\vec{k}') \frac{\mathcal{A}_0}{1+\sigma_k^2-\mathcal{A}_0^2}. \end{aligned} \quad (60)$$

For a fixed value of the wave vector \vec{k} , both correlation functions (59) and (60) have two Dirac- δ peaks. One of these is for $\vec{k}'=\vec{k}$ (self-correlation), and arises from the phase-

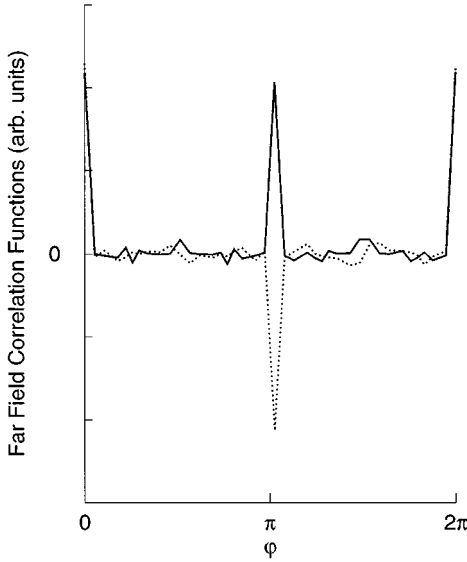


FIG. 4. Far-field correlation functions in homodyne detection versus the polar angle that spans the circle of Fig. 2 for $k^2 = -\delta_1 = 1$ and $\mathcal{A}_0 = 0.95$. The solid line corresponds to the quadrature component X while the dashed one corresponds to the component Y .

insensitive contribution (50), while the other is located at $\vec{k}' = -\vec{k}$ and arises from the phase-sensitive contribution (49). In Fig. 4 we have plotted the results of the numerical simulations for the correlation functions (59) and (60) of X and Y : both \vec{k} and \vec{k}' lie on the critical circle, \vec{k} is fixed while \vec{k}' spans the critical circle, and φ is the azimuthal angle between the two wave vectors. The correlation functions are obtained by performing a time average plus an average with respect to the position of \vec{k} over the circle. The function displays a positive (negative) peak at $\vec{k}' = -\vec{k}$ (i.e., $\varphi = \pi$) for the X (Y) quadrature. In Fig. 5 we have plotted the magnitude of the two peaks using Eqs. (59) and (60) and compared it with the results of the direct numerical simulation of the Langevin equation for values of \mathcal{A}_0 approaching threshold. The agreement establishes again the reliability of our numerical code for the simulation of the stochastic partial differential equations. The explanation of the Dirac- δ peak at $\varphi = \pi$ is quite straightforward. Two photons at the signal frequency are produced by the OPO instantaneously via an off axis emission: close to threshold the probability is maximum for emission on a cone forming an angle $\theta = k_{\text{crit}}/k_z$ with the cavity axis (which corresponds to the critical circle in the far field); although the direction of emission of the couple on the cone fluctuates in time, the two photons have to be emitted in two symmetrical directions in order to preserve the transverse momentum resulting on average in a circular emission in the far field with correlation peaks on opposite sides of the circle.

The mechanism behind the latter effect is traceable to the nature of the $\chi^{(2)}$ nonlinearity of the crystal, which gives rise to the phase-sensitive contribution (50). Note that the correlation function is maximum (in modulus) when \vec{k} lies on the critical circle (37) as happens for the mean intensity distribution (52). In comparison with the mean intensity distribu-

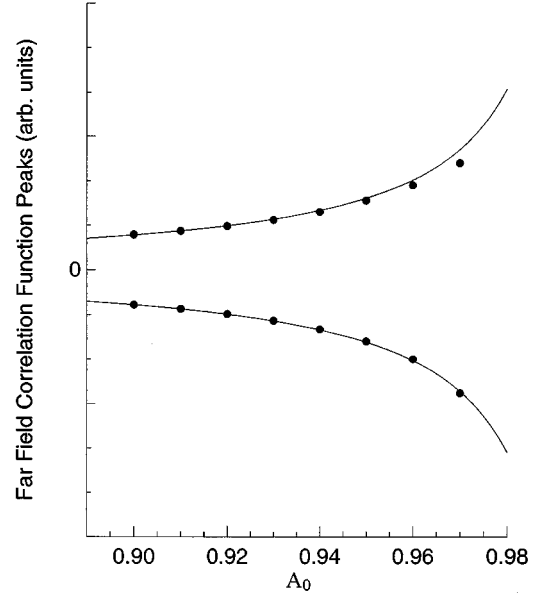


FIG. 5. Peaks of the far-field correlation functions in homodyne detection for the X quadrature (upper part) and Y quadrature (lower part) components versus the input amplitude. The solid lines are the analytical results while the dots correspond to the Langevin numerical simulations.

tion, the correlation function conveys the additional evidence of the two-photon character of the signal field emission in the OPO.

We observe finally that the quantities which have a most direct physical meaning are normally and time ordered. As a matter of fact, the measurements are usually taken out of the cavity, and the intracavity results [for example, those given by equations (49), (50), (59), and (60)] remain unchanged for the output field (apart from a trivial multiplication of each factor $\Delta\alpha_1$ and β by $\sqrt{2\gamma}$) only when they refer to normally and time-ordered quantities. The normally ordered correlation function corresponding to Eqs. (59) and (60) are obtained by subtracting a factor $\delta(\vec{k} - \vec{k}')$ from each of them.

B. Near-field correlation functions

The images and correlation functions of the far signal field below threshold reveal some of the features of the roll pattern appearing above threshold. We now turn our attention to the information contained in the near-field signal. First, it is easy to show that the mean intensity of the signal below threshold is homogeneous in space. In fact, by transforming back in real space relation (38) and using Eq. (50) one obtains

$$\begin{aligned}
 \langle A_1^\dagger(\vec{x}) A_1(\vec{x}') \rangle &= \langle \Delta\alpha(\vec{x}) \Delta\alpha^*(\vec{x}') \rangle - \frac{1}{2} \delta(\vec{x} - \vec{x}') \\
 &= \frac{1}{4\pi^2} \int d^2\vec{k} \frac{|\mathcal{A}_0|^2}{2(1 + \sigma_k^2 - |\mathcal{A}_0|^2)} e^{i\vec{k} \cdot (\vec{x} - \vec{x}')} \\
 &= \frac{1}{2\pi} \frac{|\mathcal{A}_0|^2}{\sqrt{1 - |\mathcal{A}_0|^2}} \text{Im}\{K_0(-iP|\vec{x} - \vec{x}'|)\},
 \end{aligned} \tag{61}$$

where

$$P = \sqrt{k_{\text{crit}}^2 + i(1 - |\mathcal{A}_0|^2)^{1/2}}, \quad (62)$$

K_0 is the modified Bessel function of zero order, and a is defined by Eq. (32). No information about spatial modulations can be obtained from the average near-field image since the RHS of Eq. (61) is independent of \vec{x} for $\vec{x} = \vec{x}'$. This does not mean, however, that information about the emerging pattern and about the nonclassical nature of the emitted light cannot be obtained in the near field. We define the near-field correlation functions corresponding to the homodyne detection of the signal fluctuations as

$$\begin{aligned} \Gamma_\phi(\vec{x}, \vec{x}') &= a[\langle \mathcal{E}_\phi(\vec{x}) \mathcal{E}_\phi(\vec{x}') \rangle], \\ \mathcal{E}_\phi(\vec{x}) &= \Delta \alpha_1^*(\vec{x}) e^{i\phi} + \Delta \alpha_1(\vec{x}) e^{-i\phi}, \end{aligned} \quad (63)$$

where the angle ϕ identifies the quadrature component of the field. For definiteness we now choose \mathcal{A}_0 real, so that the most significant quadratures are $\phi = 0, \pi$. By transforming back in real space and using Eqs. (59) and (60) one obtains

$$\begin{aligned} \Gamma_{\phi=0}(\vec{x}, \vec{x}') &= \frac{1}{4\pi^2} \int d^2\vec{k} \left\{ 1 + \frac{\mathcal{A}_0(1 + \mathcal{A}_0)}{1 + \sigma_k^2 - \mathcal{A}_0^2} \right\} e^{i\vec{k} \cdot (\vec{x} - \vec{x}')} \\ &= \delta(\vec{x} - \vec{x}') + \frac{1}{\pi} \frac{\mathcal{A}_0(1 + \mathcal{A}_0)}{\sqrt{1 - \mathcal{A}_0^2}} \\ &\quad \times \text{Im}\{K_0(-iP|\vec{x} - \vec{x}'|)\}, \end{aligned} \quad (64)$$

$$\begin{aligned} \Gamma_{\phi=\pi/2}(\vec{x}, \vec{x}') &= \frac{1}{4\pi^2} \int d^2\vec{k} \left\{ 1 - \frac{\mathcal{A}_0(1 - \mathcal{A}_0)}{1 + \sigma_k^2 - \mathcal{A}_0^2} \right\} e^{i\vec{k} \cdot (\vec{x} - \vec{x}')} \\ &= \delta(\vec{x} - \vec{x}') - \frac{1}{\pi} \frac{\mathcal{A}_0(1 - \mathcal{A}_0)}{\sqrt{1 - \mathcal{A}_0^2}} \\ &\quad \times \text{Im}\{K_0(-iP|\vec{x} - \vec{x}'|)\}. \end{aligned} \quad (65)$$

As a consequence of the translational symmetry, the correlation function Γ_ϕ depends only on the difference $r = |\vec{x} - \vec{x}'|$. For both values of $\phi = 0, \pi$ the correlation function has a δ function contribution for equal space points. The origin of this δ function is the diverging vacuum fluctuations associated with symmetrically ordered expectation values. This term disappears when going from the Wigner representation to the more usual Glauber-Sudarshan P representation (corresponding to normal ordering). Hence it is convenient to introduce

$$\tilde{\Gamma}_{\phi=0} = \frac{1}{\pi} \frac{\mathcal{A}_0(1 + \mathcal{A}_0)}{\sqrt{1 - \mathcal{A}_0^2}} \text{Im}\{K_0(-iP|\vec{x} - \vec{x}'|)\}, \quad (66)$$

$$\tilde{\Gamma}_{\phi=\pi/2} = -\frac{1}{\pi} \frac{\mathcal{A}_0(1 - \mathcal{A}_0)}{\sqrt{1 - \mathcal{A}_0^2}} \text{Im}\{K_0(-iP|\vec{x} - \vec{x}'|)\}, \quad (67)$$

which is the normally ordered part of the field correlation functions. Note that these analytical expressions have already been given in [14].

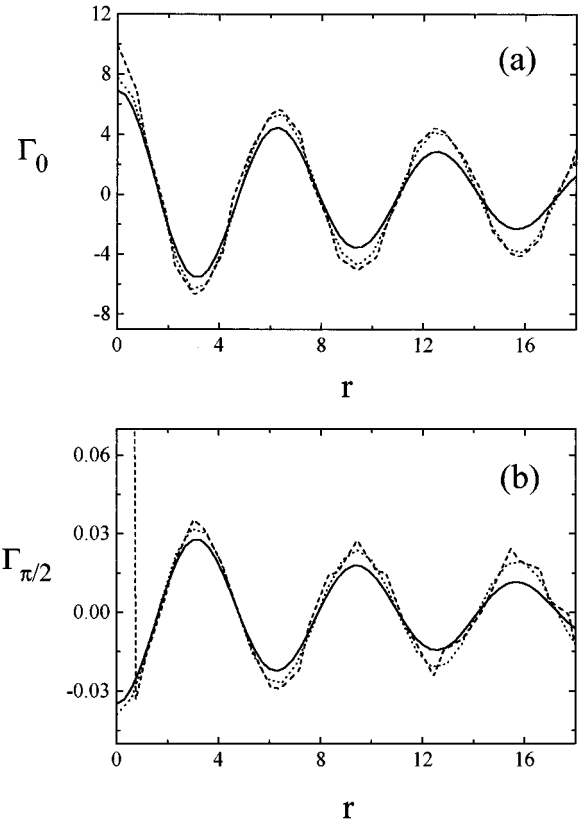


FIG. 6. Near-field spatial correlation function $\Gamma_\phi(r)$ for the antisqueezed (a) and squeezed (b) quadrature components of the signal fluctuations of an OPO below threshold. Case of one-dimensional transverse space. The solid line is the analytical result, the dashed line is obtained by the numerical simulations, and the dotted line was obtained by including finite grid effects into the analytical results. The value of the pump field is $\mathcal{A}_0 = 0.99$ while the detuning is $\delta_1 = -1$.

If instead of two transverse dimension we consider only one transverse dimension, replacing \vec{x} by x and ∇^2 by $\partial^2/\partial x^2$, instead of Eqs. (66) and (67) we have

$$\tilde{\Gamma}_{\phi=0} = \frac{1}{2} \frac{\mathcal{A}_0(1 + \mathcal{A}_0)}{\sqrt{1 - \mathcal{A}_0^2}} \text{Re} \left\{ \frac{e^{iP|x-x'|}}{P} \right\}, \quad (68)$$

$$\tilde{\Gamma}_{\phi=\pi/2} = -\frac{1}{2} \frac{\mathcal{A}_0(1 - \mathcal{A}_0)}{\sqrt{1 - \mathcal{A}_0^2}} \text{Re} \left\{ \frac{e^{iP|x-x'|}}{P} \right\}. \quad (69)$$

We see that close to threshold the critical modes, for which the effective detuning $\delta_1 + k^2$ vanishes, become dominant. This shows that the spatial modulation of the semiclassical pattern above threshold also affects the quantum correlation functions in the near field. In Fig. 6 we have plotted a comparison between the theory (solid curve) and Langevin simulations (dashed curve) of the normally ordered part $\tilde{\Gamma}$ of the near-field correlation function for $\phi = 0$ [Fig. 6(a)] and $\phi = \pi$ [Fig. 6(b)] for the case of only one transverse dimension. The full two-dimensional case is presented in Figs. 7(a) and 7(b). The modulation, which indicates an alternation between correlation and anticorrelation, has the same wavelength as the semiclassical pattern that appears above thresh-

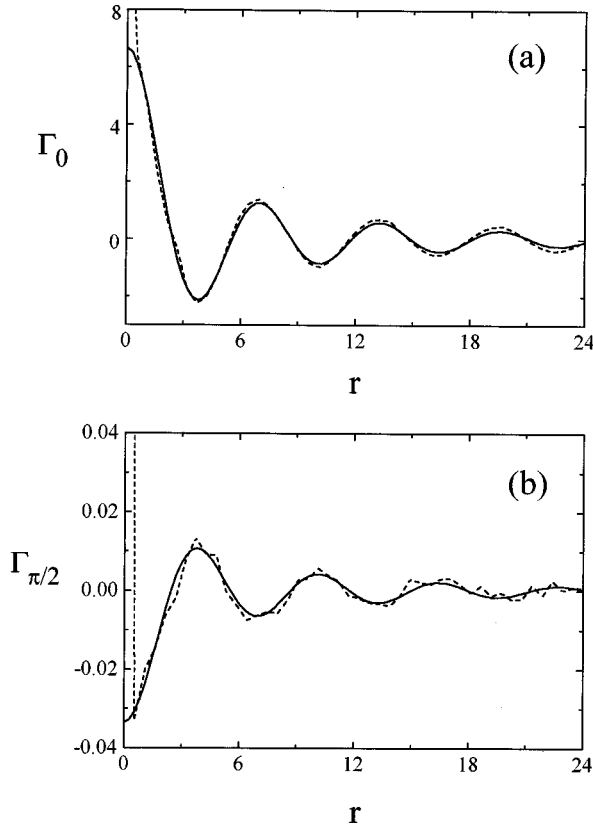


FIG. 7. Same as Fig. 6 but for the case of two-dimensional transverse space.

old and can therefore be regarded as a quantum anticipation of this pattern. The term “quantum image” was introduced by Knight *et al.* [30] to describe the encoding of information in the quantum correlation function instead of the light intensity and it therefore seems appropriate to use it for the phenomenon described here. For vanishing distance r the normally ordered correlation function of the quadrature component corresponding to $\phi=0$ is positive, so this quadrature component is antisqueezed. The normally ordered correlation function for the perpendicular quadrature component is negative, indicating the squeezing of this quadrature component [14].

The spatial modulation of the correlation function can be made clearer in the asymptotic expansion of Eqs. (64) and (65) for large $r=|\vec{x}-\vec{x}'|$:

$$\Gamma_0(r) \approx \frac{\mathcal{A}_0(1+\mathcal{A}_0)}{\sqrt{1-\mathcal{A}_0^2}} \sqrt{\frac{1}{2\pi P^2 r k_{\text{crit}}}} e^{-(\epsilon/2k_{\text{crit}})r} \times \sin(k_{\text{crit}}r + \pi/4), \quad (70)$$

$$\Gamma_{\pi/2}(r) \approx \frac{\mathcal{A}_0(1-\mathcal{A}_0)}{\sqrt{1-\mathcal{A}_0^2}} \sqrt{\frac{1}{2\pi P^2 r k_{\text{crit}}}} e^{-(\epsilon/2k_{\text{crit}})r} \times \sin(k_{\text{crit}}r - \pi/4), \quad (71)$$

where ϵ is a measure for the distance from threshold

$$\epsilon = \sqrt{(\mathcal{A}_0^{(\text{thr})})^2 - \mathcal{A}_0^2} \quad (72)$$

and P is defined in Eq. (62). This asymptotic expansion also allows us to read out directly the correlation length $\xi = 2k_{\text{crit}}/\epsilon$ which diverges as $1/\epsilon$ as threshold is approached, a behavior analogous to the critical behavior in mean field theories.

To improve the statistics in the numerical simulations, the ensemble average in Eq. (63) has been replaced by a combined time, ensemble averages, and an average with respect to the first point position \vec{x} in $\Gamma(\vec{x}, \vec{x}')$. The deviations between numerical and theoretical data in Figs. 6 and 7 can be explained as a finite grid effect. The Langevin equations are numerically integrated on a grid of size b^d where d is the dimension of the transverse space. The minimum spacing between k vectors is then $2\pi/b$, whereas the maximum k vector is $\pi/\Delta x$, Δx being the lattice spacing of the spatial grid. If we replace the integrals in Eqs. (64) and (65) with summations over k vectors, then we obtain curves almost identical to the numerical results. For example, in Fig. 6 the dotted line is the modified version of the theoretical data after including finite grid effects leading to an excellent agreement with the numerical data. In the two-dimensional case of Fig. 7 finite grid effects do not play a significant role and we did not include the dotted line. Note also the δ contribution at the origin in the numerical result due to

$$\delta(x) = \begin{cases} 1/(\Delta x)^d & \text{for } x=0, \\ 0 & \text{elsewhere,} \end{cases} \quad (73)$$

where d is the dimension of the transverse space.

It should be noted that the numerical results for the anti-squeezed quadrature component in Figs. 6(a) and 7(a) show less fluctuations than the squeezed quadrature component shown in Figs. 6(b) and 7(b). The reason is that the correlations in the latter component are generally small with respect to the large contribution for vanishing distances dominated by the δ function in Eqs. (64) and (65). Results can be improved by averaging over a longer time t or over a larger number of realizations. Increasing the number of grid points also reduces the statistical errors (because of the averages over the position) as well as the finite grid effects but can make numerical simulations unfeasibly long.

We now turn our attention to the correlation between intensity fluctuations at two different space points in the near field, a quantity which can be measured without using a local oscillator. The calculation of the intensity correlation function is simplified by taking into account the Gaussian character of the fluctuations in this Langevin model, allowing us to express higher order field moments by means of second-order moments of the fields.

For the normally ordered intensity correlation function, one obtains

$$\bar{\Gamma}_{\text{int}}(\vec{x}, \vec{x}') = a^2 [\langle A_1^\dagger(\vec{x}) A_1^\dagger(\vec{x}') A_1(\vec{x}') A_1(\vec{x}) \rangle - \langle A_1^\dagger(\vec{x}) A_1(\vec{x}) \rangle \langle A_1^\dagger(\vec{x}') A_1(\vec{x}') \rangle] \quad (74)$$

$$= a^2 [|\langle A(\vec{x}) A(\vec{x}') \rangle|^2 + |\langle A^\dagger(\vec{x}) A(\vec{x}') \rangle|^2]. \quad (75)$$

After transforming Eqs. (49) and (50) into real space, and transforming from symmetrical to normal ordering, the RHS of Eq. (75) is calculated as

$$\begin{aligned} \tilde{\Gamma}_{\text{int}}(\vec{x}, \vec{x}') &= \left\{ \frac{1}{2\pi} \mathcal{A}_0 \text{Re}[K_0(-iP|\vec{x}-\vec{x}'|)] \right\}^2 \\ &\quad + \frac{1+\mathcal{A}_0^2}{4(1+\mathcal{A}_0)^2} \left\{ \frac{1}{\pi} \frac{1+\mathcal{A}_0}{\sqrt{1-\mathcal{A}_0^2}} \right. \\ &\quad \left. \times \text{Im}[K_0(-iP|\vec{x}-\vec{x}'|)] \right\}^2 \end{aligned} \quad (76)$$

$$\approx \frac{1}{8} [\Gamma_0(\vec{x}, \vec{x}')]^2 \quad \text{for } \mathcal{A}_0 \rightarrow 1, \quad (77)$$

where P is defined by Eq. (62). The approximation (77) evidences the simple physical result that the intensity correlation function close to threshold is proportional to the square of the antisqueezed quadrature correlation function. This can be directly seen from the following formula, which can be easily verified by substitution:

$$\begin{aligned} \tilde{\Gamma}_{\text{int}}(\vec{x}, \vec{x}') &= \left[\frac{\Gamma_{\phi=0}(\vec{x}, \vec{x}') - \Gamma_{\phi=\pi/2}(\vec{x}, \vec{x}')}{4} \right]^2 \\ &\quad + \left[\frac{\Gamma_{\phi=0}(\vec{x}, \vec{x}') + \Gamma_{\phi=\pi/2}(\vec{x}, \vec{x}')}{4} \right]^2 \\ &\quad - \left[\frac{\Gamma_{\phi=\pi/4}(\vec{x}, \vec{x}') - \Gamma_{\phi=-\pi/4}(\vec{x}, \vec{x}')}{4} \right]^2. \end{aligned} \quad (78)$$

The RHS of Eq. (78) can be approximated by Eq. (77) if $\Gamma_{\phi=0}$ is much larger than the other phase quadrature correlation functions. A further advantage of expressing the intensity correlation function by means of the field correlation functions is that Eq. (78) holds also for the other model discussed later, i.e., the OPO with spherical mirrors. Moreover, the calculations taking into account the finite grid effects in the numerical simulation do not need to be repeated for the intensity correlation functions, since the results for the quadrature correlation functions can be inserted in Eq. (78) or Eq. (77).

Again, we can present a comparison of the theoretical results of the intensity correlation function with its numerical evaluation from the Langevin equations. Since the statistical average of functions of the c -number field $\Delta\alpha_1(\vec{x})$ gives the symmetrically ordered quantum expectation value, we have first to express Eq. (74) in a symmetrically ordered way:

$$\begin{aligned} \Gamma_{\text{int}}(\vec{x}, \vec{x}') &= a^2 \langle [A_1^\dagger(\vec{x}) A_1^\dagger(\vec{x}') A_1(\vec{x}') A_1(\vec{x})]_{\text{sym}} \rangle \\ &\quad - \langle (A_1^\dagger(\vec{x}) A_1(\vec{x}))_{\text{sym}} \rangle \langle (A_1^\dagger(\vec{x}') A_1(\vec{x}'))_{\text{sym}} \rangle \\ &= \tilde{\Gamma}_{\text{int}}(\vec{x}, \vec{x}') + \delta(\vec{x}-\vec{x}') \left\{ a \langle A_1^\dagger(\vec{x}) A_1(\vec{x}') \rangle \right. \\ &\quad \left. + \frac{1}{4} \delta(\vec{x}-\vec{x}') \right\}. \end{aligned} \quad (79)$$

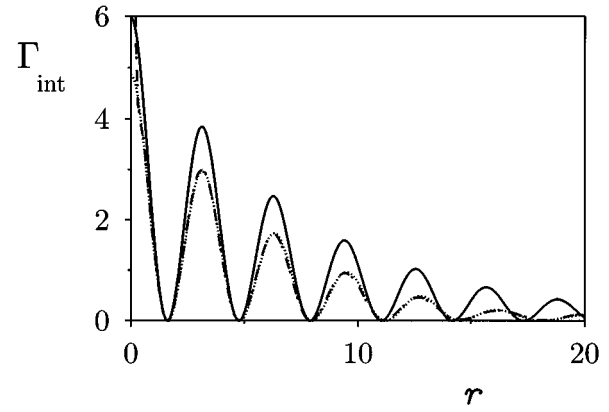


FIG. 8. Near-field intensity correlation function for the one-dimensional model for the OPO below threshold. The value of \mathcal{A}_0 is 0.99 while the detuning is $\delta_1 = -1$. The solid line is the analytical result for $\tilde{\Gamma}_{\text{int}}$, the dashed line is the numerical result for Γ_{int} , and the dotted line is a modification of the analytical result taking account for the finite grid effects in the numerical computation.

The results are shown in Figs. 8 and 9 for the one- and two-dimensional cases, respectively.

The intensity correlation function shows a modulation at half the wavelength of the field correlation functions in Figs. 6 and 7 because the intensity is the modulus square of the field. The numerical result is shown by the dashed line. Again the numerical result shows a faster decay with increasing distance $r = |\vec{x} - \vec{x}'|$ with respect to the analytical result (solid line), and this deviation can be revealed as a finite grid effect by comparison with the analytical result, where the infinite integral over \vec{k} is replaced by an appropriate sum (dotted line). The remaining difference between the dashed and the dotted line at small distance r is due to the δ function contribution in Eq. (79). We see that the intensity correlation function remains positive for all values of the distances $|\vec{x} - \vec{x}'|$, in contrast to the case of the phase quadrature correlation function, which takes on negative values at small distance for $\phi = \pi/2$. This result is expected, since it is known that in the OPO below threshold there is no intensity squeezing.

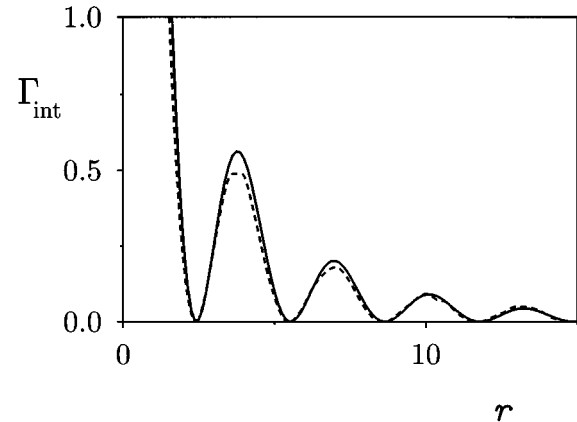


FIG. 9. Same as Fig. 8 but for the case of two-dimensional transverse space.

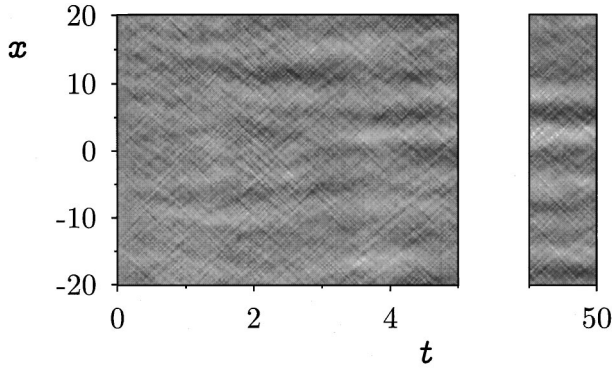


FIG. 10. Time evolution of the antisqueezed quadrature component $\mathcal{E}_{\phi=0}$ in the one-dimensional model for the OPO. The left part shows the transient starting from the uniform initial state $\Delta\alpha_1(x,0)=0$, whereas the stripe to the right shows the evolved pattern after a long time ($\tau=50$). Again the pump value is $\mathcal{A}_0=0.99$ while the detuning is $\delta_1=-1$.

Apart from the correct correlation functions, the numerical simulations provide us with images as they could be obtained by a measurement on a time scale short enough to resolve the dynamics of quantum fluctuations. For this we just have to look at a single snapshot of a field quadrature component at a given time τ .

In this connection, an important remark concerns the interpretation of the snapshots of $\text{Re}\Delta\alpha_1(\vec{x},t)$ and $\text{Im}\Delta\alpha_1(\vec{x},t)$ as corresponding to real measurements in a homodyne detection scheme. As a matter of fact the Wigner function is not a probability distribution in phase space, but its marginals are probability distributions. Hence it is correct to interpret the snapshots of $\text{Re}\Delta\alpha_1$ and $\text{Im}\Delta\alpha_1$ separately as corresponding to real measurements. It would be incorrect, however, to consider the two snapshots simultaneously to infer the instantaneous value of other quantities, such as, e.g., the intensity distribution. By construction all the snapshots refer to the intracavity field.

The one-dimensional model allows us to use a second dimension as a time axis and to code the values of the real part of $\Delta\alpha_1(x,\tau)$ in gray scales. Figure 10 shows a time evolution of the antisqueezed quadrature component of $\Delta\alpha_1(x,\tau)$ with initial conditions given by $\Delta\alpha_1(x,\tau=0)=0$. The brighter and darker shades correspond to positive and negative values of $\Delta\alpha_1(x,\tau)$, respectively. The emerging pattern shown to the extreme right of Fig. 10 is built up by quantum fluctuations; it shows a clear modulation at the wavelength $2\pi/k_{\text{crit}}$, with k_{crit} given by Eq. (37).

Figure 11 shows a snapshot of the real part of $\Delta\alpha_1(\vec{x},\tau)$ for the two-dimensional case. The underlying pattern, which in low-frequency measurements can only be revealed by measuring the correlation function, is also present in single realizations of our numerical simulation which correspond to high-frequency measurements. Figure 11 clearly shows the formation of an irregular spot pattern, built up by quantum-fluctuations. The spots perform a slow random walk in the transverse plane, consistently with the fact that the quantum-mechanical expectation value of $A_1(\vec{x})$ vanishes in all positions \vec{x} . Note that this configuration must not be confused with a standard speckle pattern, in which the statistical dis-

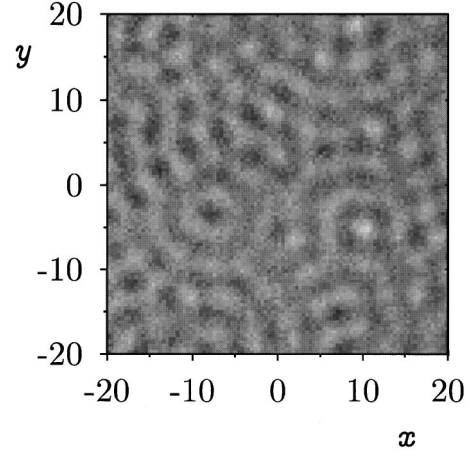


FIG. 11. Single snapshot of the antisqueezed quadrature component of the signal field in the two-dimensional OPO with plane mirrors. Darker areas correspond to negative values of $\Delta\alpha_1$ whereas positive values are shown as lighter areas. The field forms an irregular spot pattern which is built up by quantum fluctuations. Here $\mathcal{A}_0 = 0.999$ while the detuning is $\delta_1 = -1$.

tribution of distances between neighboring spots is peaked at zero distance. In our case, the peak occurs in correspondence to the wavelength $\lambda_{\text{crit}}=2\pi/k_{\text{crit}}$, and the spots manifest a sort of classical antibunching behavior in their spatial distribution. The pattern observed is similar and in fact mathematically related to the one built up by classical critical fluctuations. Unlike the classical fluctuations, however, the quantum fluctuations allow for negative values of the correlation functions at zero distance, associated with the nonclassical squeezing.

A natural question which arises is on what time scale the pattern is observable directly, for example, by means of a homodyne detection measurement with a CCD camera placed in the transverse plane. This time scale can be determined by the calculation of a temporal correlation function of the form

$$\Gamma_{\phi}(\Delta\tau)=\langle\mathcal{E}_{\phi}(x,\tau)\mathcal{E}_{\phi}(x,\tau+\Delta\tau)\rangle. \quad (80)$$

This correlation function was evaluated numerically (see Fig. 12) for the most amplified quadrature component $\mathcal{E}_{\phi=0}$ in the one-dimensional case, and shows an exponential decay $\propto\exp(\Delta\tau/\tau')$ with a long characteristic time $\tau'\approx 60$ (in scaled time units, i.e., $60\gamma_1^{-1}$ in physical units).

This decay time is in rough agreement with the expression of the decay time of the fluctuations of the critical modes, given by $\tau'=(1-\mathcal{A}_0)^{-1}$, which gives, in the present case, ≈ 50 in scaled time units (see Eq. (98) of [14]). The divergence of the decay time when approaching the threshold is closely related to the critical slowing down known from classical phase transitions. Experimentally this slowing down simplifies the direct detection of the spatial pattern, since it allows for the use of detectors with longer time scales.

We can try to extract the spatial correlation function out of a single snapshot by replacing the required ensemble average in Eq. (63) by a spatial average over the point \vec{x} keeping the difference vector $\vec{x}-\vec{x}'$ fixed. The result is shown in Fig. 13 as a function of $\vec{x}-\vec{x}'$ and shows the expected modu-

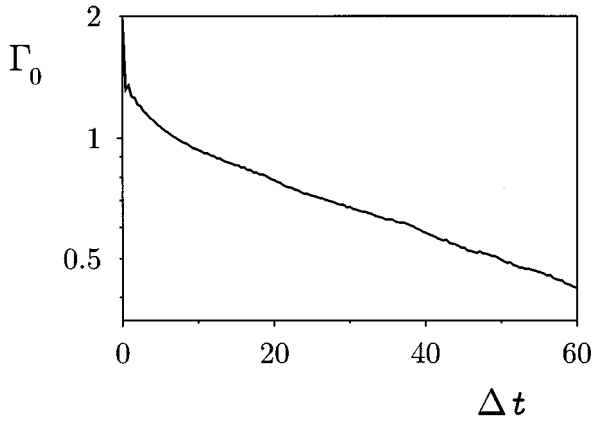


FIG. 12. Temporal correlation function $\langle \mathcal{E}_0(x, \tau) \mathcal{E}_0(x, \tau + \Delta\tau) \rangle$ in logarithmic scale as a function of the time difference $\Delta\tau$. The slow decay of this correlation indicates that the pattern is long lived. Here $\mathcal{A}_0 = 0.98$ while the detuning is $\delta_1 = -1$.

lation in $r = |\vec{x} - \vec{x}'|$. Due to the finite size of the transverse plane in the numerical simulation, the correlation function depends not only on r but also slightly on the angle of the difference vector $\vec{x} - \vec{x}'$, an effect which decreases with increasing size of the simulation grid in the transverse plane.

V. OPO CAVITY WITH PLANE MIRRORS AND AN INPUT BEAM OF FINITE DIAMETER

In the previous section we have verified that our Langevin equations (22) and (23) correctly describe the quantum fluctuations of the signal field by making a comparison between the data obtained by their numerical integration and analytical results available in the case of homogeneous input beams, plane mirrors, and below threshold. This case is, however, unrealistic for experimental realizations where input beams of finite diameter, generally of Gaussian shape, are commonly utilized. It is the aim of this section to show that quantum images and modulated spatial correlations for

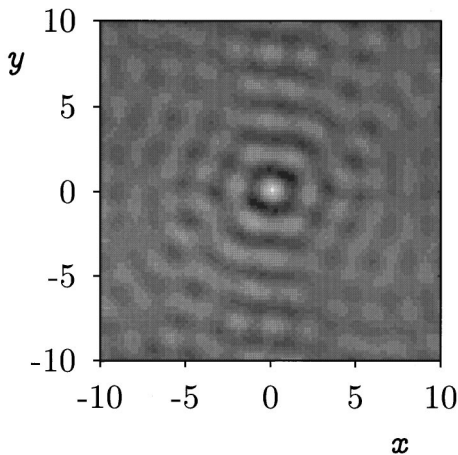


FIG. 13. The spatial correlation function of the antisqueezed quadrature component as a function of the vector $\vec{x} - \vec{x}'$. Brighter and darker parts indicate correlation and anticorrelation, respectively. One clearly sees the ring-shaped structure around the origin corresponding to the alternation of correlation and anticorrelation.

OPO's below threshold can still be observed in the case of input beams of finite diameter.

In the present case Eq. (33), valid below threshold, is modified to

$$\frac{\partial}{\partial \tau} \Delta \alpha_1(\vec{x}, \tau) = -(1 + i\delta_1 - i\nabla^2) \Delta \alpha_1(\vec{x}, \tau) + \mathcal{A}_0(\vec{x}) \Delta \alpha_1^*(\vec{x}, \tau) + \sqrt{2} \xi_1(\vec{x}, \tau), \quad (81)$$

where $\mathcal{A}_0(\vec{x})$ is the asymptotic solution of the semiclassical equation

$$\frac{\gamma_1}{\gamma_0} \frac{\partial}{\partial \tau} \mathcal{A}_0(\vec{x}) = - \left(1 + i\delta_0 - i \frac{\gamma_1}{2\gamma_0} \nabla^2 \right) \mathcal{A}_0(\vec{x}) + E(\vec{x}), \quad (82)$$

where

$$\delta_0 = \frac{\omega_0 - 2\omega_s}{\gamma_0}, \quad E(\vec{x}) = \frac{g}{\gamma_1 \gamma_0} \mathcal{E}_{\text{in}}(\vec{x}). \quad (83)$$

Note that in this case the solution of Eq. (82) is not given by Eq. (36) since diffraction plays a role in the final configuration of the pump field. For example, Fig. 14 displays the stationary distribution of the modulus and the imaginary part of $\mathcal{A}_0(\vec{x})$ for the two real input pump shapes studied here: a top-hat profile

$$E(\vec{x}) = \frac{E}{2} \{ 1 - \tanh[\nu(r - \mu)] \}, \quad (84)$$

and a Gaussian profile

$$E(\vec{x}) = E \exp\left(\frac{-2r^2}{\mu^2}\right), \quad (85)$$

where r is the transverse radial coordinate and μ and ν are shape parameters, governing the radius of the central part and the slope of the steep part for the top hat profile, respectively. The fact that the imaginary part of $\mathcal{A}_0(\vec{x})$ is not uniform is due to the diffractive term in Eq. (82) and can have drastic effects on the Langevin simulations of the signal field. Equation (81) differs from Eq. (33) in that it is a stochastic partial differential equation with space-dependent coefficients. Simple transformations to the Fourier space to perform analytical calculations similar to that presented in the previous section are now unfeasible and one has to rely on the numerical simulations. From the numerical-integration point of view, the term multiplied by the space-dependent parameter has to be treated like a nonlinear term and requires a high degree of accuracy. For example, numerical methods based on the Euler discretization of the Laplacian operator are bound to fail and to produce spurious results [31]. For these reasons all the results of this section have been obtained by using a stochastic split-step numerical integration routine with second-order accuracy in time. Integrations have been performed on dedicated workstations and could easily take several CPU hours for each run.

Figure 15 shows that the far-field quantum image survives for both cases of top-hat ($E = 0.97$) and Gaussian ($E = 1.0$) profiles and should be visible in experiments. Note that the

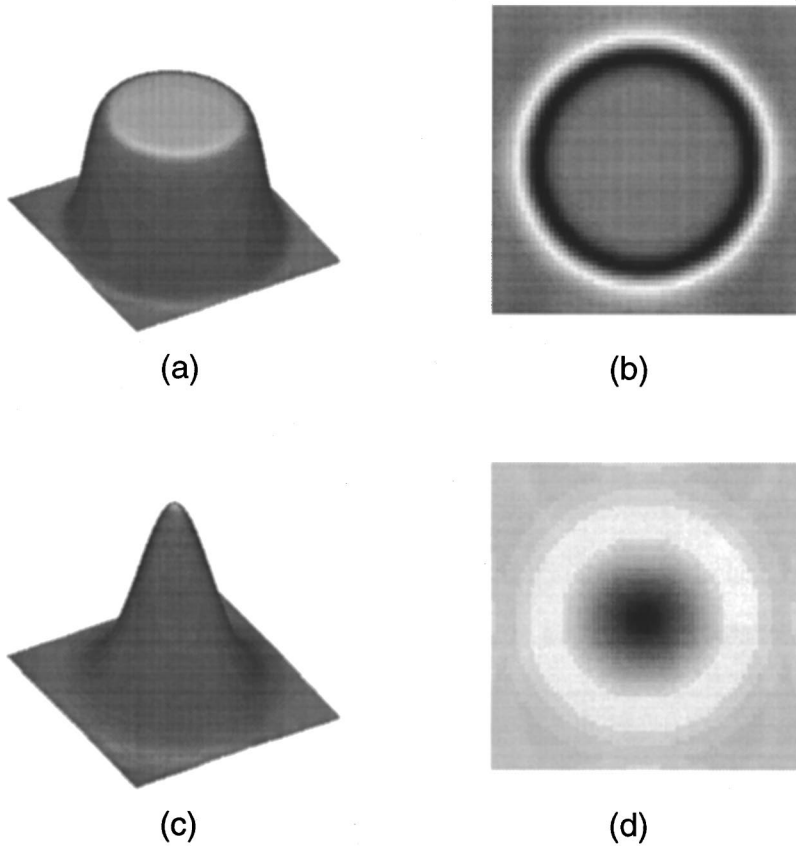


FIG. 14. Intensity profiles of the stationary pump field \mathcal{A}_0 for the case of top-hat (a) and Gaussian (c) input beam shapes. Panels (b) and (d) show the imaginary part of \mathcal{A}_0 where white (black) corresponds to positive (negative) values. Parameters are $\delta_0=0$, $\gamma_1/\gamma_0=1$, $E=0.97$, $\nu=0.4547$, and $\mu=18.85$ for the top-hat profile and $\delta_0=0$, $\gamma_1/\gamma_0=1$, $E=1.0$, and $\mu=11.75$ for the Gaussian profile.

Gaussian profile tends to favor spatial areas where the pump field is far from threshold and consequently reduces the visibility of the quantum image. Correlation at opposite sides of the far-field ring [see Eqs. (59) and (60)] are still detectable in the presence of input beams of finite diameter even if the reduced visibility of the Gaussian profile case can make these measurements difficult to be performed. We note that, in the case of input beams of finite diameter it is not necessary to use a lens to observe the far field. The far-field configuration arises at a distance from the cavity much larger than μ^2/λ , where μ is the beam size and λ the wavelength.

Figures 16 and 17 show the near-field correlations obtained from the numerical integration of Eq. (81) for the top-hat and Gaussian profiles, respectively, compared with the case of homogeneous pump. In the top-hat case, the points \vec{x} and \vec{x}' are both taken in the flat upper part, and the correlation function is obtained by performing an average

over time and an average with respect to \vec{x} over the flat upper part. In the Gaussian case, the point \vec{x} is fixed at $\vec{x}=0$ and the correlation function is obtained by an average over time only.

Oscillations in the antisqueezed component of the near-field correlations are clearly detectable even for Gaussian input pumps. The squeezed component of the near-field correlations, however, drastically deteriorates for the case of Gaussian input fields and may be impossible to be characterized in real experiments.

VI. OPO CAVITY WITH SPHERICAL MIRRORS

The standard experimental realizations of OPO systems utilize cavities with spherical mirrors instead of plane mirrors (see Fig. 18). This case was already treated in Ref. [16]. We assume, that the pump field is not reflected by the cavity

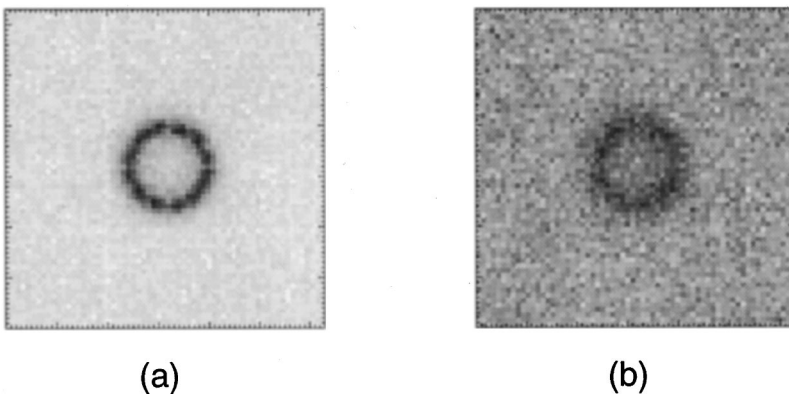


FIG. 15. Time average of the far-field intensity of the signal fluctuations for top-hat (a) and Gaussian (b) input profiles. Higher intensities correspond to darker areas. The detuning of the signal is $\delta_1 = -1$. Other parameters are as in Fig. 14.

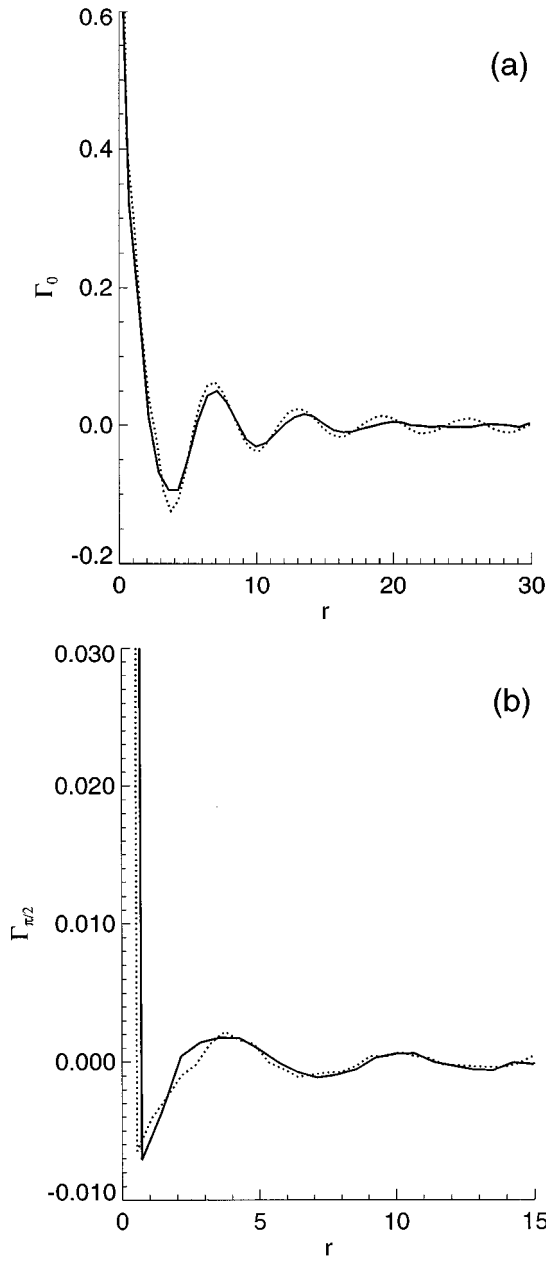


FIG. 16. Near-field spatial correlation function $\Gamma_\phi(r)$ for the antisqueezed (a) and squeezed (b) quadrature components of the signal field of an OPO below threshold. Comparison between the case of top-hat (solid line, $E=0.97$) and homogeneous input beams (dashed line, $\mathcal{A}_0=0.97$). The parameters for the top-hat case are as in Fig. 14 and $\delta_1 = -1$ in both cases.

mirrors and has a plane wave configuration, and that the Rayleigh length of the cavity is much larger than the cavity length. This implies that the frequency spacing between adjacent transverse modes is much smaller than that between adjacent longitudinal modes (free spectral range). This amounts to the requirement that the cavity mirrors are quasiplanar. The realization with spherical mirrors has the advantage that there is a discrete basis of eigenfunctions, namely the Gauss-Laguerre modes. The complete set of eigenfunctions is given by

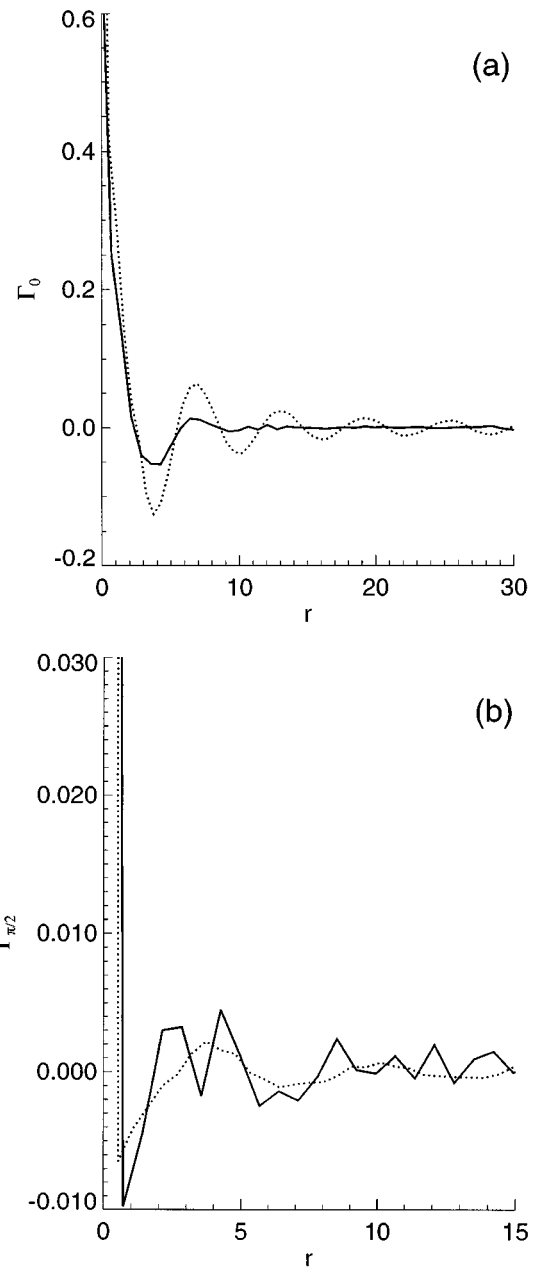


FIG. 17. Near-field spatial correlation function $\Gamma_\phi(r)$ for the antisqueezed (a) and squeezed (b) quadrature components of the signal field of an OPO below threshold. Comparison between the case of Gaussian (solid line, $E=1.0$) and homogeneous input beams (dashed line, $\mathcal{A}_0=0.97$). The parameters for Gaussian case are as in Fig. 14 and $\delta_1 = -1$ in both cases.

$$f_{pli}(r, \varphi) = \frac{2}{[2^{\delta_{l,0}} \pi]^{1/2}} (2r^2)^{1/2} \left[\frac{p!}{(p+l)!} \right]^{1/2} \times L_p^l(2r^2) e^{-r^2} \begin{cases} \cos l\varphi & \text{for } i=1, \\ \sin l\varphi & \text{for } i=2, \end{cases} \quad (86)$$

where r denotes the distance from the axis of the system, normalized to the beam width in the fundamental Gaussian

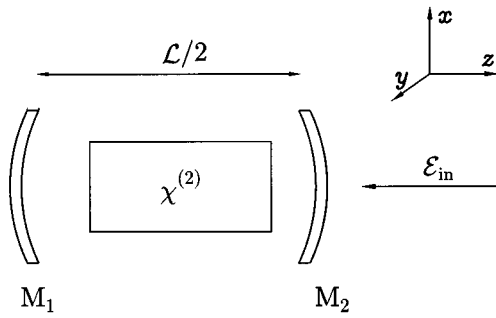


FIG. 18. Experimental setup for an OPO with spherical mirrors. The nonlinear optical crystal is inside a cavity with spherical mirrors which is pumped with light of frequency $2\omega_s$. The crystal down-converts this light to frequency ω_s , which is then detected.

mode. It will turn out to be convenient to split these mode functions into their angular parts;

$$f_{li}^{(1)}(\varphi) = \begin{cases} \cos l\varphi & \text{for } i=1, \\ \sin l\varphi & \text{for } i=2, \end{cases} \quad (87)$$

and into the rest $f_{pl}^{(2)}(r)$ which has only a radial dependence. The eigenfrequencies of these modes depend only on the family index $q = 2p + l$:

$$\omega_{pl} = \omega_1 + \eta(2p + l), \quad (88)$$

where η is determined by the distance between the spherical mirrors and their radius of curvature. In the limit of vanishing curvature of the mirrors, the spacing η tends to zero resembling the continuous spectrum in the case of plane mirrors. Of special interest is the case where $(\omega_s - \omega_1)/\eta$ is a positive integer, since there exists a family of modes which are exactly in resonance with the signal field. This family is characterized by

$$q = q_{\text{crit}} = \frac{\omega_s - \omega_1}{\eta}. \quad (89)$$

Any state can be expanded into the modes (86)

$$\Delta\alpha_1(r, \varphi, t) = \sum_{pli} \beta_{pli}(t) f_{pli}(r, \varphi). \quad (90)$$

The classical behavior of an OPO with spherical mirrors is similar to one with plane mirrors in the sense that by increasing the pump intensity the system undergoes a second-order phase transition. Immediately above threshold, the spatial configuration of the signal field is determined exclusively by the modes with the smallest effective detuning

$$\Delta_{pl} = \frac{\omega_{pl} - \omega_s}{\gamma_1} = \Delta_{00} + (2p + l) \frac{\eta}{\gamma_1}, \quad (91)$$

which are the most unstable ones; as we will see these modes dominate also the ‘‘quantum image’’ built up by quantum fluctuations below threshold. For example, when condition (89) is satisfied the pattern is determined by the family $q = q_{\text{crit}}$, and this is again closely similar to the plane wave case, in which there is a critical wave vector determined by

the resonance condition $\sigma_k = 0$ [see Eq. (37)] identical to that which leads to the definition of the critical family index q_{crit} , i.e., $\Delta_q = 0$.

Below threshold the Langevin equations for the expansion coefficients β_{pli} read in scaled time units [compare with Eq. (33)]

$$\frac{d}{d\tau} \beta_{pli}(\tau) = -(1 + i\Delta_{pl}) \beta_{pli}(\tau) + \mathcal{A}_0 \beta_{pli}^*(\tau) + \sqrt{2} \xi_{pli}(\tau). \quad (92)$$

The noise terms ξ_{pli} are δ correlated in time and mode indices:

$$\langle \xi_{pli}^*(\tau) \xi_{p'l'i'}(\tau') \rangle = \frac{1}{2} \delta_{p,p'} \delta_{l,l'} \delta_{i,i'} \delta(\tau - \tau'), \quad (93)$$

$$\langle \xi_{pli}(\tau) \xi_{p'l'i'}(\tau') \rangle = 0. \quad (94)$$

By performing calculations closely similar to those of Sec. IV A, one can obtain time evolution equations for the second-order moments

$$C_1(p, l, i; p', l', i'; \tau) = \langle \beta_{pli}(\tau) \beta_{p'l'i'}(\tau) \rangle, \quad (95)$$

$$C_2(p, l, i; p', l', i'; \tau) = \langle \beta_{pli}^*(\tau) \beta_{p'l'i'}(\tau) \rangle \quad (96)$$

of the mode amplitudes. The asymptotic values for $\tau \rightarrow \infty$ are given by

$$C_1(p, l, i; p', l', i') = \frac{\mathcal{A}_0(1 - i(\Delta_{pl}))}{2(1 - |\mathcal{A}_0|^2 + \Delta_{pl}^2)} \delta_{pp'} \delta_{ll'} \delta_{ii'}, \quad (97)$$

$$C_2(p, l, i; p', l', i') = \frac{1 + \Delta_{pl}^2}{2(1 - |\mathcal{A}_0|^2 + \Delta_{pl}^2)} \delta_{pp'} \delta_{ll'} \delta_{ii'}. \quad (98)$$

From this we obtain the stationary spatial correlation function

$$\Gamma_\phi(r, \varphi, r', \varphi') = \langle \mathcal{E}_\phi(r, \varphi) \mathcal{E}_\phi(r', \varphi') \rangle \quad (99)$$

for the quadrature components

$$\mathcal{E}_\phi(r, \varphi) = \sum_{pli} f_{pli}(r, \varphi) (\beta_{pli} e^{-i\phi} + \beta_{pli}^* e^{i\phi}). \quad (100)$$

In the special cases $\phi = 0$ and $\phi = \pi/2$ (most antisqueezed and most squeezed quadrature component, when \mathcal{A}_0 is real) we obtain

$$\Gamma_{\phi=0}(r, \varphi, r', \varphi') = \sum_{pli} \left(1 + \frac{\mathcal{A}_0(1 + \mathcal{A}_0)}{1 - \mathcal{A}_0^2 + \Delta_{pl}^2} \right) f_{pli}^{(2)}(r) f_{pli}^{(2)}(r') \cos[l(\varphi - \varphi')], \quad (101)$$

$$\Gamma_{\phi=\pi/2}(r, \varphi, r', \varphi') = \sum_{pli} \left(1 - \frac{\mathcal{A}_0(1 - \mathcal{A}_0)}{1 - \mathcal{A}_0^2 + \Delta_{pl}^2} \right) f_{pli}^{(2)}(r) f_{pli}^{(2)}(r') \cos[l(\varphi - \varphi')]. \quad (102)$$

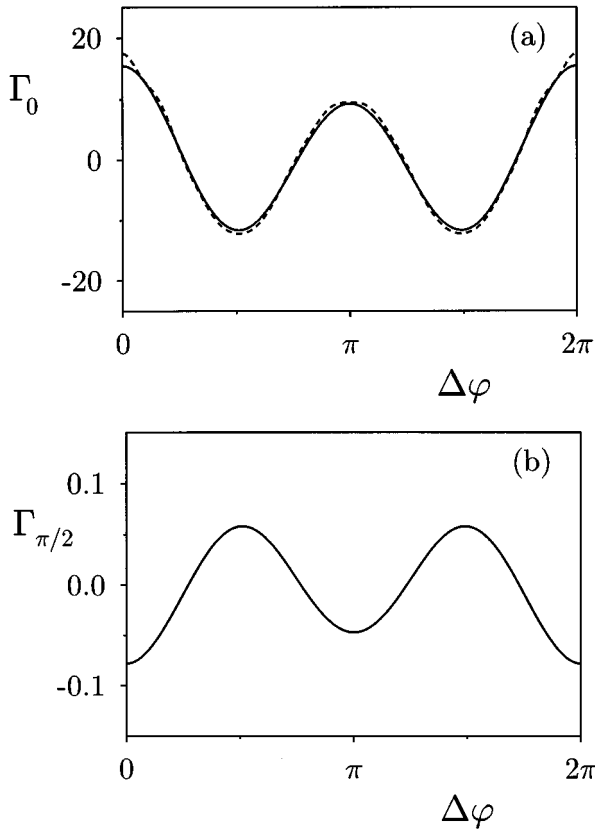


FIG. 19. The two-point field correlation function Γ_ϕ in the case of the OPO with spherical mirrors is plotted as a function of the angular separation $\Delta\phi$ between the two points. Both points have radial coordinate $r=r'=2^{-1/2}$. The most antisqueezed quadrature component ($\phi=0$) is shown in (a), whereas (b) shows the most squeezed component ($\phi=\pi/2$). The solid line in both plots show the analytical result and the dotted line in (a) shows for comparison the numerical result.

These correlation functions were calculated in [16] in the P representation. As in the case of plane mirrors we get a δ contribution from the 1 in the sum over all modes, reflecting the fact that we deal with symmetrically ordered expectation values (Wigner representation). Again this term vanishes on passing to the more usual normal ordering. As for the case of plane mirrors for pump field intensities close to the threshold ($1-A_0^2 \ll 1$) the critical modes with $2p+l=q_{\text{crit}}$ become dominant in the sums (101) and (102). The results (101) and (102) for $r=r'=\sqrt{2}$, $\Delta_{00}=-1$, $\eta/\gamma_1=0.5$, and $A_0=0.99$ are shown as a function of $\Delta\phi$ in Fig. 19 as solid lines; the numerical results obtained solving Eq. (92) are shown as a dashed curve. Both quadrature component correlations exhibit a noteworthy modulation, despite the fact that the mean intensity is uniform over the circle, for a fixed r . We already subtracted the δ contribution from both numerical and analytical results; for a finite number of included families this is a large contribution even for $\Delta\phi \neq 0$. In the case of the squeezed quadrature component the numerical data suffer from the fact that they appear as the difference of two large, almost identical numbers: the symmetrically ordered correlation function, which is the outcome of the numerical simulation, and the δ contribution. With the restricted number of

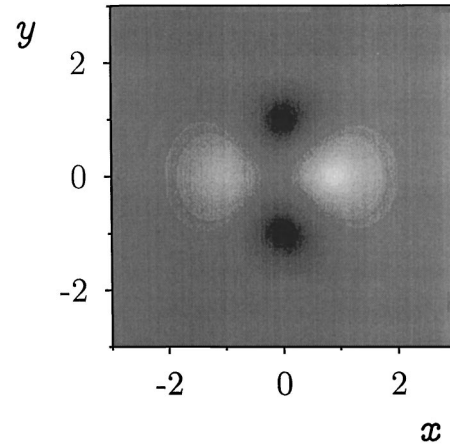


FIG. 20. The two-point field correlation function of the most antisqueezed quadrature component as a gray scale plot (bright parts indicate correlation and dark parts anticorrelation). One of the two points is fixed, whereas the other one explores the whole transverse plane, and the correlation is plotted as a function of the Cartesian coordinates (x,y) of this second point.

realizations the fluctuations in these numbers do not allow for an accurate extraction of the underlying normally ordered part of the correlation function, therefore we did not include the numerical result in Fig. 19(b). Figure 20 shows a two-dimensional plot of the correlation function of the anti-squeezed quadrature component, for the same values of the parameters. For the calculation of the intensity correlation function we can refer to the expression (75), and make use of Eqs. (95) and (96); the normally ordered part of this function is given by

$$\begin{aligned} \tilde{\Gamma}_{\text{int}}(r, \phi, r', \phi') = & \frac{A_0^2}{4} \sum_{pl} \sum_{p'l'} \frac{(1+i\Delta_{pl})(1-i\Delta_{p'l'}) + A_0^2}{(1-A_0^2+\Delta_{pl}^2)(1-A_0^2+\Delta_{p'l'}^2)} \\ & \times f_{pl}^{(2)}(r)f_{pl}^{(2)}(r')f_{p'l'}^{(2)}(r)f_{p'l'}^{(2)}(r') \\ & \times \cos[l(\phi-\phi')]\cos[l'(\phi-\phi')]. \quad (103) \end{aligned}$$

This result together with the numerically obtained intensity correlation function is shown in Fig. 21. Because the intensity correlation function is essentially the square of the field correlation function the deviation of the analytical and numerical results is even larger than in the case of the field correlation function (Fig. 19).

Again we can also present single realizations to give an impression of what one can expect to get in high-frequency measurements. By choosing $A_0=0.999$, $\Delta_{00}=-1$ and for a separation of the modes $\eta/\gamma_1=-\Delta_{00}/2$, we obtain a picture as presented in Fig. 22(a)—the underlying pattern is almost invisible. The reason for this disappointing result is that the pattern is restricted to a small area around the optical axis and includes only two significant “spots” with negative (brighter parts) and two with positive values (darker parts), respectively. The correlation function in Fig. 20 shows us that there is nothing more to expect. Therefore it is not possible to observe a large number of spots as it was in the case of plane mirrors, where the number of spots is only restricted

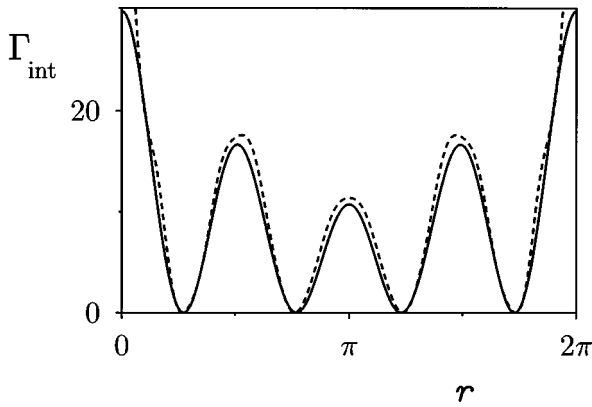


FIG. 21. The intensity correlation function for the OPO with spherical mirrors as a function of the angular separation between the two points, on a circle of radius $r=2^{-1/2}$ around the optical axis. Again we show the analytical result (solid line) and the numerical result (dashed line). The pump field amplitude is $A_0=0.99$ and the detuning and mode spacing are $\Delta_{00}=-1$ and $\eta/\gamma_1=0.5$.

by the size of the simulation square in the transverse plane. In order to make the regularity of the pattern visible also in single snapshots one has to reduce the value of the intermode spacing η , which corresponds to an experiment with less curved mirrors. In this case the number of spots increases and, e.g., for a value of $\eta/\gamma_1=0.1|\Delta_{00}|$ one obtains even for a reduced pump intensity ($A_0=0.99$) the picture shown in Fig. 22(b).

We note that all the results presented here refer to the near field; the far-field picture displays some noteworthy features analogous to what is discussed in Sec. IV A for the plane mirror case and which will be reported in a separate publication [32].

VII. CONCLUSIONS

We have shown that semiclassical patterns arising in non-linear optical systems above certain thresholds are anticipated in the far-field mean intensity of the output field and in the near-field quantum correlation function already below threshold. To demonstrate this we examined in detail the case of a degenerate OPO with plane and spherical mirrors. In both cases the far-field intensity, the correlation of typical quadrature components, and the intensity correlations show the spatial modulation which characterizes the semiclassical pattern. Since main analytical results about near-field correlations were already presented by some of us elsewhere [14,16], we have focused here on the numerical simulation of stochastic partial differential equations of the Langevin type for the quantum fluctuations and on the far-field distributions and correlations. The agreement between numerical and analytical results is excellent and allows for a safe use of the numerical Langevin equations to regimes where no direct comparison with the theory is possible. For example, we have analyzed here the case of space-dependent pump profiles and found that modulations in the correlation functions may be difficult to detect in real experiments while the features of the far-field images are more robust. On the other hand, correlation functions carry a larger amount of informa-

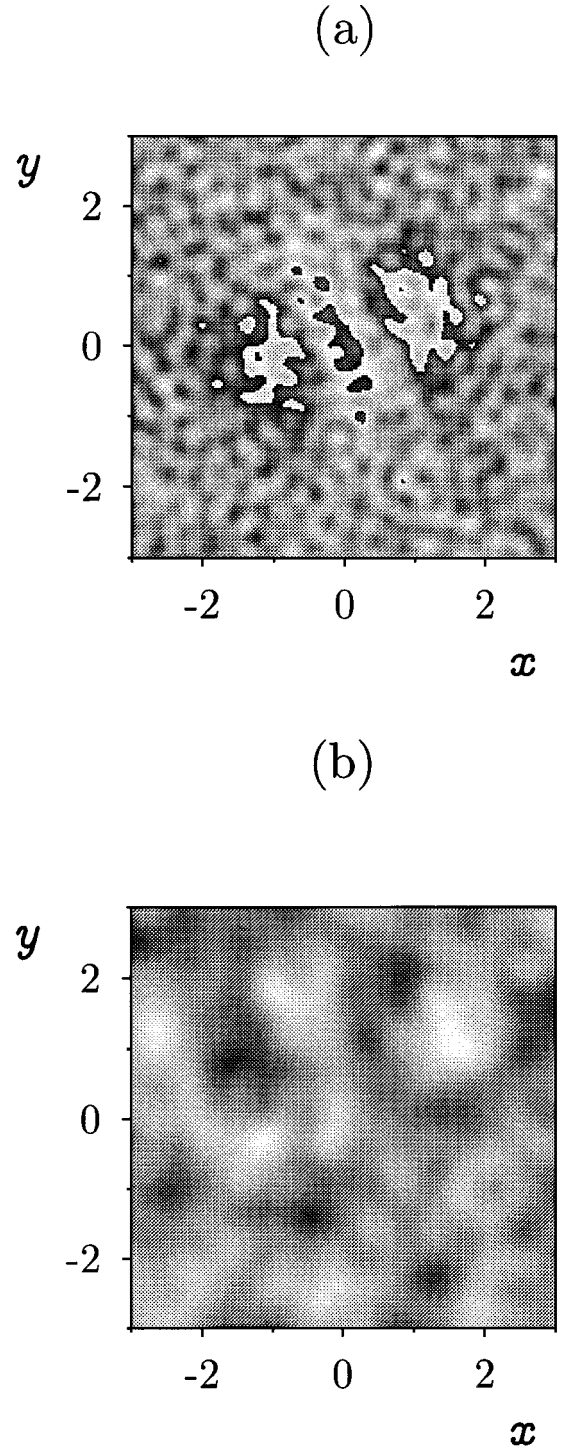


FIG. 22. Snapshot of the antisqueezed quadrature component in the OPO with spherical mirrors. The pump field amplitude is $A_0=0.999$ for (a) and $A_0=0.99$ for (b). For the snapshot shown in (a) $\eta/\gamma_1=-0.5\Delta_{00}=0.5$, while in (b) $\eta/\gamma_1=-0.1\Delta_{00}=0.1$.

tion than averages, which do not exhibit any structure with respect to the angular variable in the transverse plane.

We have also shown that not only measurements of the correlation functions but also short time measurements of the near field reveal the incoming spatial modulation. For the experimentally relevant case of an OPO with spherical mirrors we showed that the spatial pattern is visible in the latter kind of measurements only for nearly flat mirrors.

ACKNOWLEDGMENTS

We are grateful to M. Giglio and J. Jeffers for stimulating discussions. This work was supported in part by the European Union Human Capital Mobility (Network Nonclassical Light) and Training and Mobility of Researchers (Network Quantum Structures FMRX-CT96-0077) and by the United Kingdom Engineering and Physical Sciences Research Council (Grant No. K/70212).

APPENDIX

Let us consider for simplicity a one-dimensional version of the stochastic differential equation (27) (the generalization to the multidimensional case is straightforward):

$$dX(t) = -\alpha X(t) + dB(t), \quad (\text{A1})$$

where $dB(t)$ are Wiener increments. The formal integration of the equation (A1) from $t=0$ up to a generic time t is given by

$$X(t) = \exp(-\alpha t)X(0) + \int_0^t \exp[-\alpha(t-t')]dB(t'), \quad (\text{A2})$$

where $X(0)$ is a given starting point of the stochastic process X . Our aim is to find a discrete algorithm to perform the stochastic Ito integral [33]

$$A(t) = \int_0^t f(t-t')dB(t'), \quad f(t) = \exp(-\alpha t), \quad (\text{A3})$$

in such a way that the statistical average $\langle X^2(t) \rangle$ is evaluated with a given accuracy. The same accuracy affects also the evaluation of the correlation function, since the latter is related to the variance by the deterministic formula

$$\langle X(t+\tau)X(t) \rangle = \exp(-\alpha\tau)\langle X(t)X(t) \rangle.$$

Let $t_0=0, t_1, t_2, \dots, t_{N+1}=t$ be a partition of the interval $(0, t)$ with $\Delta t = t_{j+1} - t_j$. We set

$$\int_0^t f(t-t')dB(t') \approx \sum_{j=0}^N G_j [B(t_{j+1}) - B(t_j)], \quad (\text{A4})$$

where the generic coefficients G_j 's are chosen in such way that the accuracy of the numerical evaluation of $\langle A^2(t) \rangle$ is maximized. One has the identity (see, e.g., [33] p. 19)

$$\langle A^2(t) \rangle = \left\langle \left[\int_0^t f(t-t')dB(t') \right]^2 \right\rangle = \int_0^t f^2(t-t')dt'. \quad (\text{A5})$$

By using the property of the Wiener increments $\langle [B(t_{j'+1}) - B(t_{j'})][B(t_{j+1}) - B(t_j)] \rangle = \delta_{j,j'}\Delta t$, it follows that

$$\langle A^2(t) \rangle = \sum_{j=0}^N G_j^2 \Delta t. \quad (\text{A6})$$

Hence, the maximum accuracy in the evaluation of $\langle A^2(t) \rangle$ is obtained by selecting

$$G_j^2 = \tilde{G}_j^2 := \frac{1}{\Delta t} \int_{t_j}^{t_{j+1}} dt' f^2(t'). \quad (\text{A7})$$

We can expand \tilde{G}_j in power of Δt up the first order as

$$\tilde{G}_j^2 = e^{-2\alpha(t-t_j)} \frac{e^{2\alpha\Delta t} - 1}{2\alpha\Delta t} = e^{-2\alpha[t-(t_j+t_{j+1})/2]} + O(\Delta t^2), \quad (\text{A8})$$

$$\tilde{G}_j = e^{-\alpha[t-(t_j+t_{j+1})/2]} + O(\Delta t^2). \quad (\text{A9})$$

By inserting the approximation (A9) in Eqs. (A4) and (A2) a recursive algorithm to perform the stochastic time evolution of X is obtained:

$$X(t_n) = e^{-\alpha\Delta t}X(t_{n-1}) + e^{-\alpha\Delta t/2}[B(t_n) - B(t_{n-1})] \quad (\text{A10})$$

with an error of the order Δt^2 in the evaluation of $\langle X(t)^2 \rangle$. This is exactly the same formula as Eq. (30) of Sec. II, provided one makes the correspondence: $t_{n-1} \rightarrow t$, $t_n \rightarrow t + \Delta t$ $[B(t_n) - B(t_{n-1})] \rightarrow \int_t^{t+\Delta t} dt' \Theta(t')$, $-\alpha \rightarrow \mathbf{L}_{\text{det}}$.

[1] J. Mod. Opt. **34** (1987), special issue on *Squeezed Light*, edited by R. Loudon and P. L. Knight. In particular, see the introductory article of the editors.
[2] J. Opt. Soc. Am. B **4** (1987), special issue on *Squeezed States of the Electromagnetic Field*, edited by H. J. Kimble and D. F. Walls.
[3] Appl. Phys. B **55** (1992), special issue on *Quantum Noise Reduction in Optical Systems/ Experiments*, edited by C. Fabre and E. Giacobino.
[4] J. Opt. Soc. Am. B **7**, 948 (1990), special issue on *Transverse Effects in Nonlinear Optical Systems*, edited by N. B. Abraham and W. J. Firth; **7**, 1764 (1990).
[5] L. A. Lugiato, Phys. Rep. **219**, 293 (1992); C. O. Weiss, *ibid.* **218**, 311 (1992).
[6] Chaos Solitons Fractals **4**, 1249 (1994), special issue on *Nonlinear Optical Structures, Patterns, and Chaos*, edited by L. A. Lugiato.

[7] M. I. Kolobov and I. V. Sokolov, Sov. Phys. JETP **69**, 1097 (1989); Phys. Lett. A **140**, 101 (1989); Europhys. Lett. **15**, 271 (1991).
[8] A. La Porta and R. E. Shusher, Phys. Rev. A **44**, 2013 (1991).
[9] P. Kumar and M. I. Kolobov, Opt. Commun. **104**, 374 (1994).
[10] L. Mandel and E. Wolf, *Optical Coherence and Quantum Optics* (Cambridge University Press, Cambridge, 1995).
[11] L. A. Lugiato and F. Castelli, Phys. Rev. Lett. **68**, 3284 (1992).
[12] G. Grynberg and L. A. Lugiato, Sov. Phys. Crystallogr. **101**, 69 (1993).
[13] L. A. Lugiato and A. Gatti, Phys. Rev. Lett. **70**, 3868 (1993).
[14] A. Gatti and L. A. Lugiato, Phys. Rev. A **52**, 1675 (1995).
[15] L. A. Lugiato and G. Grynberg, Europhys. Lett. **29**, 675 (1995).
[16] L. A. Lugiato and I. Marzoli, Phys. Rev. A **52**, 4886 (1995).
[17] G.-L. Oppo, M. Brambilla, and L. A. Lugiato, Phys. Rev. A **49**, 2028 (1994); G.-L. Oppo, M. Brambilla, D. Camesasca, A.

- Gatti, and L. A. Lugiato, *J. Mod. Opt.* **41**, 1151 (1994).
- [18] V. Degiorgio and M. O. Scully, *Phys. Rev. A* **2**, 1170 (1970).
- [19] R. Graham and H. Haken, *Z. Phys.* **237**, 31 (1970).
- [20] P. D. Drummond, K. J. McNeil, and D. F. Walls, *Opt. Acta* **28**, 211 (1981).
- [21] C. W. Gardiner, *Quantum Noise* (Springer, Berlin, 1991).
- [22] H. Carmichael, *An Open Systems Approach to Quantum Optics*, edited by F. S. Bastich, *Lecture Notes in Physics* Vol. 18 (Springer, Berlin, 1993).
- [23] C. Cohen-Tannoudji, J. Dupont-Roc, and G. Grynberg, *Atom-Photons Interactions* (Wiley, New York, 1995).
- [24] K. E. Cahill and R. J. Glauber, *Phys. Rev.* **177**, 1882 (1969).
- [25] R. P. Feynman and A. R. Hibbs, *Quantum Mechanics and Path Integrals* (McGraw-Hill, New York, 1965).
- [26] R. J. Rivers, *Path Integral Methods in Quantum Field Theory* (Cambridge University Press, Cambridge, 1987).
- [27] S. M. Barnett, *Phys. Rev. A* **43**, 6418 (1991).
- [28] S. Reynaud, A. Heidmann, E. Giacobino, and C. Fabre, *Prog. Opt.* **30**, 1 (1992).
- [29] A. C. Newell and J. V. Moloney, *Nonlinear Optics* (Addison-Wesley, Redwood City, CA, 1992).
- [30] P. L. Knight *et al.* (unpublished).
- [31] W. H. Press, S. A. Teukolsky, W. T. Vetterling, and B. P. Flannery, *Numerical Recipes* (Cambridge Press, Cambridge, 1992).
- [32] I. Marzoli, A. Gatti, and L. A. Lugiato (unpublished).
- [33] B. Oksendal, *Stochastic Differential Equations* (Springer, Berlin, 1992).